

Aerosol deposition in mucus-lined ciliated airways

Swarnaditya Hazra¹ and Jason R. Picardo¹†

¹Department of Chemical Engineering, Indian Institute of Technology Bombay, Mumbai 400076, India

We study the transport and deposition of inhaled aerosols in a mid-generation, mucus-lined lung airway, with the aim of understanding if and how airborne particles can avoid the mucus and deposit on the airway wall—an outcome that is harmful in case of allergens and pathogens but beneficial in case of aerosolized drugs. We adopt the weighted-residual integral boundary-layer model of Dietze and Ruyer-Quil (*J. Fluid Mech.*, vol. 762, 2015, pp. 68–109) to describe the dynamics of the mucus-air interface, as well as the flow in both phases. The transport of mucus induced by wall-attached cilia is also considered, via a coarse-grained boundary condition at the base of the mucus. We show that the capillary-driven Rayleigh-Plateau instability plays an important role in particle deposition by drawing the mucus into large annular humps and leaving substantial areas of the wall exposed to particles. We find, counter-intuitively, that these mucus-depleted zones enlarge on increasing the mucus volume fraction. Our simulations are eased by the fact that the effects of cilia and air turn out to be rather simple: the long-term interface profile is slowly translated by cilia and is unaffected by the laminar airflow. The streamlines of the airflow, though, are strongly modified by the non-uniform mucus film, and this has important implications for aerosol entrapment. Particles spanning a range of sizes (0.1 to 50 microns) are modelled using the Maxey-Riley equation, augmented with Brownian forces. We find a non-monotonic dependence of deposition on size. Small particles diffuse across streamlines due to Brownian motion, while large particles are thrown off streamlines by inertial forces—particularly when air flows past mucus humps. Intermediate-sized particles are tracer-like and deposit the least. Remarkably, increasing the mucus volume need not increase entrapment: the effect depends on particle-size, because more mucus produces not only deeper humps that intercept inertial particles, but also larger depleted-zones that enable diffusive particles to deposit on the wall.

Key words: pulmonary fluid mechanics, thin films, particle/fluid flow

1. Introduction

The air we inhale brings along a variety of harmful aerosol particles—allergens such as dust and pollen, pollutants like soot, and droplets laden with pathogens—which if deposited on the walls of the airways can cause severe respiratory illnesses (Beelen *et al.* 2014). Furthermore, particles that reach the terminal airways and alveoli can pass into the bloodstream and harm other organs, including the brain and heart (Fu *et al.* 2019; Weichenthal 2012). The lung’s primary defence against airborne particles is provided by mucus which lines the walls of lung airways (Knowles & Boucher 2002; Randell & Boucher 2006). The viscous mucus lies atop a sublayer of watery, periciliary liquid (PCL), which bathes a carpet of wall-attached cilia. The tips of the cilia penetrate the bottom of the mucus layer and transport it upward and out of the lungs, thereby evacuating particles that deposit on the mucus (Sleigh *et al.* 1988).

The lungs contain a hierarchy of 24 generations of branching tubular airways, which may be divided into three broad categories: the upper, middle, and terminal airways, corresponding to

† Email address for correspondence: picardo@iitb.ac.in

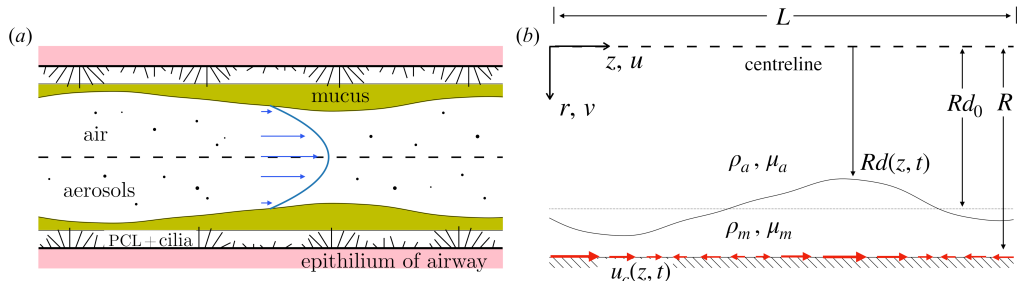


FIG. 1. (a) Illustration of a middle generation, mucus-lined, ciliated airway with inhaled aerosols being transported by the respiratory airflow. (b) Schematic of the simplified axisymmetric airway, corresponding to the mathematical model of §2. The subscripts a and m denote the air and mucus phases, respectively, and u_c is the spatio-temporally periodic, metachronal velocity (red arrows) imposed by the cilia on the base of the mucus film.

generations 0 to 9, 10 to 16, and 17 to 23, respectively (Kleinstreuer & Zhang 2010; Tsuda *et al.* 2013). From the perspective of pulmonary fluid mechanics, these categories are distinguished by the airflow regime (laminar or turbulent), the distribution and composition of the surface liquid, the compliance of the wall, and the presence or absence of cilia. In this work, we focus on a single segment of the middle airways—mucus-bearing, relatively rigid, and ciliated—and study the mucus-entrapment or wall-deposition of airborne particles (see figure 1a).

In the middle airways, the airflow is laminar with a Reynolds number between 1 to 30, in contrast to the large upper airways where the airflow is turbulent or transitional (Kleinstreuer & Zhang 2010; Tsuda *et al.* 2013). Though laminar, the airflow in middle airways can be rather complex, owing to the presence of the mucus film, which occupies a substantial portion of the airway. Here, the mucus volume fraction is typically about 10% and can increase further under diseased conditions (Levy *et al.* 2014). (Mucus is absent from the terminal airways and its volume fraction is relatively small in the upper airways (Sleigh *et al.* 1988)) A key aspect of this two-phase mucus-air flow is the annular interface, which, being endowed with interfacial tension, is susceptible to the Rayleigh-Plateau instability (Johns & Narayanan 2002). The mucus film, therefore, is spontaneously driven toward a strongly nonuniform distribution: at low volume fractions the film collects into large annular humps separated by depleted zones (Lister *et al.* 2006), while at higher volume fractions the film can form liquid bridges that block the airway (Everett & Haynes 1972). The Rayleigh-Plateau instability also produces strong transverse pressure-gradients that cause soft-walled terminal airways to collapse (Heil *et al.* 2008); such collapse does not occur in the middle airways thanks to its relatively rigid walls.

This physical picture of a typical middle airway is completed by cilia, which are present throughout the upper and middle airways (Levy *et al.* 2014). Immersed in the low-viscosity PCL, the cilia move synchronously as a metachronal wave with asymmetric forward and backward strokes—the tips of the cilia reach upward and penetrate the bottom of the mucus layer only during the forward stroke (Sleigh *et al.* 1988). Under healthy conditions, the stratified arrangement of mucus atop PCL is maintained by a network of crosslinked polymers, within the PCL, that prevents the entry of large molecular-weight mucins (Button *et al.* 2012). Thus, as a first approximation, it is reasonable to reduce the airway surface liquid to just a single film of mucus with a non-deforming base (Romanò *et al.* 2022), at which it experiences ciliary forces. The surface of this film is free to deform in response to the action of interfacial tension and airflow (see figure 1b).

Clearly, the middle airways present a challenging fluid mechanical problem, one that spans a wide range of length and time scales (see table 1). The flow and particle transport therein play an important role in respiratory diseases, because (i) if harmful particles pass through untrapped, then they will enter deep into the lungs where there is no mucus barrier, and (ii) oversecretion

Property	Typical value	Reference
<i>length scales</i>		
airway diameter	1 mm	Pedley (1977)
mucus layer thickness	0.01	Sleigh <i>et al.</i> (1988)
PCL layer thickness	0.005	Sleigh <i>et al.</i> (1988)
cilia height	0.005	Sleigh <i>et al.</i> (1988)
metachronal-wavelength	0.03	Fulford & Blake (1986)
airway length	5 – 10	Sleigh <i>et al.</i> (1988)
wavelength of RP instability	3	
distance travelled by a tracer per breathing cycle	3	
<i>velocity scales</i>		
	mm s ⁻¹	
celerity of ciliary wave	0.3	
mucociliary transport velocity	0.05	Vasquez <i>et al.</i> (2016); Oldenburg <i>et al.</i> (2012)
air velocity	10	Tsuda <i>et al.</i> (2013)
<i>time scales</i>		
	s	
cilia-beat time period	0.1	Chatelin & Poncet (2016)
breathing time period	1	Pedley (1977)
mucociliary transport time (across airway length)	100	
non-dimensional numbers	[-]	
air Reynolds number	1 – 30	Pedley (1977)
mucus Reynolds number	10 ⁻³	
air-mucus viscosity ratio	10 ⁻⁴ – 10 ⁻³	Erken <i>et al.</i> (2022)
air-mucus density ratio	10 ⁻³	Erken <i>et al.</i> (2022)

TABLE 1. Typical magnitudes of various length, velocity, and time scales in a mid-generation airway, highlighting the multiscale nature of the associated transport phenomena.

of mucus or airway constriction, triggered by the deposition of inhaled allergens (Gauvreau *et al.* 2015), can produce mucus plugs that obstruct airflow. Plugs form more easily in the smaller middle-airways (as compared to the larger upper-airways) because of the relatively large volume fraction of mucus and the relatively weak airflow, which struggles to expel the mucus plugs. Such plugs are commonly observed in cases of rapid-onset, fatal asthma (Hays & Fahy 2003; Rogers 2004). The most effective treatment for asthma, and related diseases like chronic bronchitis, involves inhalation of aerosolized drugs such as bronchodilators that relax the muscles of the airways (Rogers 2004; Williams & Rubin 2018). In this flipped scenario, the mucus film limits the efficacy of inhalation therapy (Lansley 1993), which requires that drug particles avoid mucus-entrapment and deposit on exposed sections of the airway wall.

Despite its importance, flow in the middle airways has not received much attention, possibly because it involves the simultaneous interaction of air, mucus, and cilia (Levy *et al.* 2014). Most previous studies have focused either on mucus transport by cilia (ignoring air and capillary dynamics of the interface) or air-mucus dynamics (ignoring cilia). The former combination is acceptable for the upper airways where the mucus volume fraction is too low to obstruct the airflow, while the latter combination is certainly relevant to terminal airways which are devoid of cilia. The middle airways, however, require all three factors to be considered together, which is what we do here, albeit with simplifying assumptions. Knowledge of the air-mucus flow allows

us to track the motion of air-borne particles and study their deposition on the cilia-transported, non-uniform mucus film. We thus address the following questions: (i) Does the Rayleigh-Plateau instability, which yields a non-uniform mucus distribution of humps and depleted zones, aid mucus-entrapment or facilitate wall-deposition? (ii) How do changes in the mucus volume-fraction affect particle deposition? (iii) What is the effect of the particle's size on its entrapment?

Before proceeding, though, it is useful to briefly summarize our current understanding of the three physical processes that are central to the lung's particle-trapping-evacuation system: (a) capillary-driven film dynamics, (b) mucociliary transport, and (c) particle deposition.

An annular film on the inner wall of a cylindrical tube is driven by the Rayleigh-Plateau instability to one of two morphologies. At low volume fractions, the film accumulates into unduloids, i.e. equilibrium-shaped annular humps or collars, which are separated by depleted zones that are devoid of liquid. For volume fractions beyond a critical value, unduloid solutions cease to exist and instead the film forms liquid bridges (Everett & Haynes 1972). Not only do these bridges block the airway, their formation is associated with strong recoil forces which can damage the cells of the airway wall (Romanò *et al.* 2019; Erken *et al.* 2022). Several studies have therefore analysed liquid-bridge formation, considering the effects of mucus rheology (Romanò *et al.* 2021; Erken *et al.* 2023) and surfactants (Romanò *et al.* 2022). If the wall is soft, as in the terminal airways, closure can occur even at lower volume fractions, because the capillary-induced reduction of pressure inside liquid humps causes the wall to collapse (Heil *et al.* 2008). Here, we are interested in non-collapsing, rigid-walled airways with mucus fractions that are low enough to avoid closure. Even so, the Rayleigh-Plateau instability remains important because it controls the sizes of mucus humps and depleted zones. On the one hand, humps protrude into the airway and may intercept airborne particles; on the other hand, depleted zones leave the wall exposed to particle deposition. We shall see that the net outcome of these competing effects depends on the size of the particles.

Does airflow alter the distribution of mucus? Because mucus has a much higher density and viscosity (table 1), the influence of airflow on the morphology of the film is restricted to the upper airways, where the airflow is turbulent. In the extreme case of a cough or sneeze, rapidly flowing air can rip off droplets of mucus from the film (Mittal *et al.* 2020; Morawska *et al.* 2022). In the middle airways, though, the airflow is laminar and too weak, under normal breathing conditions, to appreciably influence the morphology of the mucus film. (Our simulations, in § 3.2, confirm this assessment.) So, we include respiratory airflow in the present work not for its influence on the mucus film but to track the motion of airborne particles through the airway.

Mucociliary transport depends on the asymmetric and synchronous beating of wall-attached cilia. Each cilium executes a periodic three-dimensional motion with a quick upright forward stroke, and a slow bent-over backward stroke (Sleigh *et al.* 1988; Blake 2001). This motion is produced by internal active forces exerted by molecular motors (Gilpin *et al.* 2020) and is influenced by the flexibility of the cilium, as well as hydrodynamic interactions between segments of the cilium with each other and with the wall. Inter-cilia hydrodynamic interactions play an important role in establishing a phase-shifted synchronization that produces a metachronal wave which sweeps across the carpet of cilia (Mitran 2007; Guo *et al.* 2018; Gsell *et al.* 2020); the details of this complex fluid-structure interaction problem continue to be investigated (Chakrabarti & Saintillan 2019; Chakrabarti *et al.* 2022). Studies of mucociliary transport have typically imposed this synchronized pattern of motion onto model cilium and then calculated the resulting mucus flow (Smith *et al.* 2008). Early work, pioneered by Blake, treated the cilium using a string of Stokeslets (Smith *et al.* 2007a, 2009; Smith 2018), while more recent work has used techniques like the immersed boundary method (Sedaghat *et al.* 2016). Models have also progressed from considering just the mucus phase to including both the PCL and mucus layers (Vanaki *et al.* 2020; Quek *et al.* 2018). The computational expense of discrete-cilia models has motivated the formulation of parsimonious coarse-grained models in which explicit cilia are replaced by a force

distribution (Smith *et al.* 2007*c,b*) or a boundary condition at the base of the mucus (Vasquez *et al.* 2016; Bottier *et al.* 2017*a*). Such a simple ciliary forcing has been used to compute large-scale flow patterns (Vasquez *et al.* 2016) and to gain analytical insight into the role of viscoelasticity (Choudhury *et al.* 2023). We shall adopt the boundary-condition representation of cilia here as well.

Mucus is certainly non-Newtonian with viscoelastic properties (Levy *et al.* 2014). Its viscoelasticity plays a crucial role during rapid flows, such as the capillary-driven flow associated with airway closure and reopening (Romanò *et al.* 2021). Here, we focus primarily on open airways with relatively low mucus volumes; the corresponding slow thin-film flow is not strongly affected by viscoelasticity (Halpern *et al.* 2010). Even with cilia-driven oscillatory forcing, Choudhury *et al.* (2023) have shown that the effects of viscoelasticity are marginal under healthy conditions (with diseased mucus there is a reduction in mucociliary transport). So, for simplicity, we henceforth neglect viscoelasticity.

Particle deposition in the lungs has been measured experimentally and found to depend strongly and non-monotonically on the size of the particles, with minimal deposition at intermediate sizes (Heyder *et al.* 1986; Morawska *et al.* 2022). The physical mechanism that drives deposition varies with particle size (Guha 2008), which ranges from about 5 nm to 50 μm , and with the generation of the airway (Tsuda *et al.* 2013). The smallest particles, which are strongly affected by Brownian forces, diffusive across air streamlines and deposit on the wall or mucus. This diffusive deposition of tiny particles is relevant throughout the lungs. Intermediate-sized particles behave like tracers, following air streamlines, and so deposit the least (Tsuda *et al.* 2013).

The larger particles are unaffected by Brownian forces but deviate from streamlines due to their inertia. Whenever air streamlines are curved, inertial particles will experience cross-streamline centrifugal forces that could thrust them towards the wall (Guha 2008). Indeed, inertial deposition is known to be important in the upper airways, where the turbulent flow is strongly vortical, and at airway bifurcations, where secondary circulations are present (Kleinstreuer & Zhang 2010; Tsuda *et al.* 2013). (Centrifugal ejection of inertial particles from vortices (Maxey 1987) has been well-studied in the context of turbulent suspensions, such as droplet-laden warm clouds, for its role in accelerating collisions (Grabowski & Wang 2013; Ravichandran *et al.* 2020)). In this study, we will show that inertial deposition is relevant even in straight middle-airways, where the airflow is laminar, because of the presence of mucus humps which force the air streamlines to curve around them.

In the terminal airways, the airflow is too weak for inertial forces to play a role. Instead, gravity aids in the deposition of large particles. In the higher generations, though, gravity is unimportant, being overwhelmed by inertia and air-drag, in case of large particles, or Brownian forces, in case of small particles (Tsuda *et al.* 2013).

Simulations of particle deposition in the lungs are challenging because of complex airway geometries and air flow fields. Nevertheless, computational studies have been carried out for the nasal passage (Wang *et al.* 2009; Keeler *et al.* 2016; Farnoud *et al.* 2020), the trachea and upper conducting airways (Li & Ahmadi 1995; Lin *et al.* 2007; Rahimi-Gorji *et al.* 2015), and airway bifurcations (Hegedüs *et al.* 2004; Kleinstreuer & Zhang 2010; Ghorui *et al.* 2024). In these cases, the flow is typically turbulent or transitional. At the other end, transport in the terminal alveoli-bearing ducts of the pulmonary acinus has also received much attention (Tsuda *et al.* 2013); in fact, realistic simulations have been performed in computational geometries constructed by imaging rat lungs (Tsuda *et al.* 2008). In the alveoli, where the airflow is in the creeping regime, particle transport is facilitated by chaotic advection (Tsuda *et al.* 2002, 2011; Kumar *et al.* 2024).

The question of how the mucus film affects particle deposition has largely been overlooked, with the exception of a few studies (Aghaei *et al.* 2023), including the important work by Kim and coworkers: In a pair of studies, one *in vitro* (Kim & Eldridge 1985) and the other *in vivo* (Kim *et al.* 1985), they show that the presence of the mucus film increases the rate of particle deposition.

These studies consider an upper-generation bronchus and find that the relatively rapid airflow produces waves on the mucus film. In the middle airways, with which we are here concerned, the airflow is nearly a hundred times slower under normal breathing conditions (Tsuda *et al.* 2013); so we do not expect waves to form on the film. Nonetheless, we expect the mucus film, with its humps and depleted zones, to impact particle deposition by altering the path of airflow and the surface area for deposition.

We address this multiscale problem using long-wave reduced-order modelling techniques, along with various simplifying assumptions. The airway is modelled as a straight, rigid, cylindrical tube. The mucus layer is treated as a Newtonian viscous liquid film lining the inner cylindrical wall. The ciliary forcing to the base of the mucus is modelled as a time-dependent velocity boundary condition at the wall, designed to mimic the asymmetric metachronal wave of the cilia. Non-penetration is also imposed at the wall considering that, in healthy airways, mucus is prevented from entering the PCL sub-layer by a network of cross-linked polymers (Button *et al.* 2012). Thus, like many prior models of the airway surface liquid (*e.g.*, Romanò *et al.* 2019; Erken *et al.* 2023), we subsume the PCL-cilia layer into the wall and solve only for the dynamics of the mucus layer. The coupled flow of air and mucus—and the dynamics of the interface—is described by the two-phase thin film equations obtained from the weighted-residual integral boundary layer (WRIBL) method of (Dietze & Ruyer-Quil 2015). This method improves upon traditional long-wave lubrication theory and consistently accounts for (i) inertia up to $Re \sim 10$ (Dietze & Ruyer-Quil 2013), as occurs in the air, (ii) longitudinal viscous stresses which are relevant in thinning necks of the viscous mucus film (Dietze & Ruyer-Quil 2015), and (ii) nonlinear interfacial curvature which is crucial for realising airway closure. The WRIBL model has been extensively validated against direct numerical simulations, including for core-annular air-mucus flow (Dietze & Ruyer-Quil 2013, 2015). We further assume an axisymmetric flow field that is periodic in the longitudinal direction.

Particles are evolved assuming one-way coupling with air and ignoring inter-particle collisions (dilute limit). Within the point-particle approximation, their motion is described by the simplified Maxey-Riley equation for tiny heavy spherical particles (Maxey & Riley 1983; Ravichandran *et al.* 2017), augmented by Brownian noise. The resulting Langevin equation can be used for the full range of inhaled aerosols, with the relative strength of Brownian and inertial forces being determined by the particle size (Tsuda *et al.* 2013).

The mathematical model is presented in §2; certain simplifying limits of the model are also discussed, along with the corresponding numerical solution procedures. Section 3 focuses on just the air-mucus flow without particles. We show that interfacial deformation is driven by capillary forces and is unaffected by air (whose viscosity and density are much smaller than mucus) and ciliary transport; the latter only produce a slow lateral transport of the deformed film. These findings allow us to simplify the model and thereby ease subsequent computations.

Next, in §4, we take up the important question of how the extent of depleted zones—which expose the airway wall to particles—varies with the mucus volume fraction. The variation, measured from a number of randomly initialized simulations, is counter-intuitive: increasing the mucus volume fraction increases the extent of depleted zones. This behaviour is shown to arise from the manner in which equilibrium unduloids change shape as their volume increases.

Particle deposition is examined in §5, considering two scenarios, distinguished by the extent of particle turnover after each breath. The typical distance travelled by a particle in a breathing cycle is less than the length of an airway (table 1); so particles could remain within the same airway for many breathing cycles. However, inhalation and exhalation will bring fresh particles into the airway and remove old ones; mixing with upstream and downstream airways will also contribute to the turnover of particles (Altshuler *et al.* 1959; Wang 2005, chap 5). To aid understanding, we study the two opposing extremes: (i) particles initially introduced into the airway remain within the airway throughout the simulation and no new particles are introduced, *i.e.*, there is no particle

turnover; (ii) particles are completely replaced after every breath. Simulations are performed for dozens of breathing cycles (about a minute of breathing). Starting with the first scenario, we characterize the non-monotonic dependence of deposition on particle size and highlight the effect of the mucus volume fraction. The results are explained in terms of the physical mechanisms of Brownian and inertial cross-stream motion, and the distribution of particles in the airway. This understanding carries over to the second scenario, which reveals the effects of respiratory particle-turnover.

In the concluding §6, we summarize the key results and discuss their implications for future work.

2. Mathematical model

2.1. Long-wave equations

We model the airway as a straight cylindrical tube of radius R , lined by an annular film of mucus, which is assumed to be a Newtonian fluid with viscosity μ_m and density ρ_m . Air of viscosity μ_a and density ρ_a flows through the core. The mucus film interacts with air through an interface that is endowed with interfacial tension γ . We assume axisymmetry and adopt a cylindrical coordinate system (see figure 1b). The axial length scale Λ that characterizes axial variations is assumed to be much larger than the radius R so that $\epsilon = R/\Lambda$ is a small parameter. We can then treat the two-phase flow in the thin film limit and obtain simplified long-wave equations. Following Dietze & Ruyer-Quil (2015), we scale the continuity and Navier-Stokes equations and retain terms up to $\mathcal{O}(\epsilon^2)$ to obtain the following non-dimensional, long-wave, boundary-layer equations (Kalliadasis, Ruyer-Quil, Scheid & Velarde 2012) for pressure, p_i , and the radial and axial velocities, v_i and u_i :

$$\frac{1}{r}\partial_r(rv_i) + \partial_z u_i = 0, \quad (2.1)$$

$$\begin{aligned} \epsilon Re_i (\partial_t u_i + v_i \partial_r u_i + u_i \partial_z u_i) = -\partial_z (p_i|_d) - \epsilon^2 \partial_z (\partial_z u_i|_d) + \frac{1}{r} \partial_r (r \partial_r u_i) \\ + 2\epsilon^2 \partial_{zz} u_i + G_i \sin(\omega t), \end{aligned} \quad (2.2)$$

where all variables are non-dimensional, and ∂_t represents the partial derivative with respect to time t , and so on for ∂_r and ∂_z . The interface between the air and mucus (denoted by subscripts $i = a, m$) is located at $r = d(z, t)$. The two terms evaluated at the interface, *i.e.* those involving $p_i|_d$ and $u_i|_d$, were obtained by substituting for $\partial_z p_i$ the expression obtained after integrating the $\mathcal{O}(\epsilon^2)$ radial momentum equation from r to d .

The following characteristic scales (decorated by *) have been used for non-dimensionalization:

$$r^* = R, \quad z^* = \Lambda, \quad t^* = R/U, \quad d^* = R, \quad u_i^* = U, \quad v_i^* = \epsilon U, \quad p_i^* = \frac{\mu_i U}{\epsilon R}, \quad (2.3)$$

where U , the common velocity scale for both phases, will be chosen shortly.

The last term of (2.2) arises from the imposition of an oscillatory body force (or a background, uniform, axial pressure-gradient) in the air phase ($G_m = 0$), of frequency $f_b = \omega/2\pi$ and dimensional amplitude $A = G_a \mu_a U/R^2$, to mimic respiratory airflow. We now select the velocity scale U based on the airflow, by setting $G_a = 1$ so that $U = AR^2/\mu_a$. Then, the non-dimensional Reynolds numbers, $Re_i = \rho_i UR/\mu_i$, become $Re_a = \rho_a AR^3/\mu_a^2$ and $Re_m = Re_a \Pi_\mu/\Pi_\rho$, where $\Pi_\mu = \mu_a/\mu_m$ and $\Pi_\rho = \rho_a/\rho_m$ are the viscosity and density ratios.

Next, we list the conditions at the boundaries, starting with the interface, $r = d(z, t)$, where we require the velocities to be continuous,

$$u_a = u_m, \quad v_a = v_m, \quad \text{at } r = d, \quad (2.4)$$

and apply the $O(\epsilon^2)$ balances of tangential and normal stresses:

$$\partial_r u_m - \Pi_\mu \partial_r u_a = [2\epsilon^2 \partial_z d (\partial_z u_m - \partial_r v_m) - \epsilon^2 \partial_z v_m] - \Pi_\mu [2\epsilon^2 \partial_z d (\partial_z u_a - \partial_r v_a) - \epsilon^2 \partial_z v_a], \quad (2.5)$$

$$p_m - \Pi_\mu p_a = -Ca(\kappa) + 2\epsilon^2 (\partial_r v_m - \partial_r u_m \partial_z d) - 2\epsilon^2 \Pi_\mu (\partial_r v_a - \partial_r u_a \partial_z d), \quad (2.6)$$

where $Ca = \gamma/\mu_m U$ is the capillary number and the mean-curvature κ to $O(\epsilon^2)$ is given by

$$\kappa = \frac{1}{d} - \frac{\epsilon^2 (\partial_z d)^2}{2d} - \epsilon^2 \partial_{zz}. \quad (2.7)$$

This nonlinear approximation of the full curvature is essential for capturing the onset of liquid-bridge formation (Dietze & Ruyer-Quil 2015), which limits the volume of mucus that can be occupied in an open airway; we will show later that nonlinear curvature also has an important effect on the extent of mucus-depleted zones at the wall. In fact, the primary reason we retain terms up to $O(\epsilon^2)$ is to consistently include these effects of nonlinear curvature in the model.

The evolution of the interface is governed by the kinematic boundary condition:

$$\partial_t d = v_m - u_m \partial_z d. \quad (2.8)$$

At the centreline, we have the symmetry condition,

$$v_a = 0, \quad \partial_r u_a = 0, \quad \text{at } r = 0, \quad (2.9)$$

while at the wall, we apply the non-penetration condition and impose a tangential velocity to account for mucociliary transport:

$$v_m = 0, \quad u_m = u_c(z, t), \quad \text{at } r = 1. \quad (2.10)$$

The function $u_c(z, t)$ is a travelling wave, chosen to mimic the asymmetric metachronal wave of the cilia carpet:

$$u_c(z, t) = \begin{cases} a_f \langle u_c \rangle \sin(2\pi(z - ct)/\lambda_c) & n\lambda_c \leq z - ct < n\lambda_c + \lambda_c/2 \\ a_r \langle u_c \rangle \sin(2\pi(z - ct)/\lambda_c) & n\lambda_c + \lambda_c/2 \leq z - ct < n\lambda_c + \lambda_c \end{cases}, \quad (2.11)$$

for $n = 0, 1, 2, \dots$. The celerity of the wave is given by $c = f_c \lambda_c$ where λ_c is the metachronal wave length and f_c is the cilia-beating frequency. The mean cilia velocity, $\langle u_c \rangle = \frac{1}{\lambda_c} \int_0^{\lambda_c} u_c(z', t) dz' = \frac{1}{f_c} \int_0^{f_c} u_c(z, t') dt'$, is a non-zero constant because the forward stroke is stronger than the reverse stroke, *i.e.*, the ratio of the constants a_f/a_r is greater than unity.

This cilia boundary condition is similar to that used by Vasquez *et al.* (2016) to model cilia-driven large-scale swirling flows, observed in an *in vitro* experiment. However, while Vasquez *et al.* (2016) use a spatially invariant boundary velocity, we have used a travelling wave to better represent the metachronal cilia motion. Our boundary prescription is also closely related to that developed and validated by Bottier *et al.* (2017*b*) and used recently by Choudhury *et al.* (2023) to understand the influence of viscoelasticity on mucociliary transport; this is a Navier-slip condition that contains a slip length, which when set to zero yields a Dirichlet boundary condition just like ours. We proceed with a zero-slip condition for simplicity. As demonstrated below, the cilia-induced velocity is much too slow to alter the shape of the film or the streamlines of the airflow, and so our results regarding particle deposition will not change with the addition of slip or other modifications to the precise form of the cilia boundary condition.

To ease computations, we shall later explore whether the travelling-wave cilia-velocity can be replaced by just its mean value $\langle u_c \rangle$; the resulting Couette boundary condition is

$$v_m = 0, \quad u_m = \langle u_c \rangle, \quad \text{at } r = 1. \quad (2.12)$$

In the axial direction, we consider periodic boundary conditions. Thus, the interface profile

Parameter	Unit	Symbol	Value	Reference
airway radius	mm	R	0.4	Romanò <i>et al.</i> (2022); Weibel <i>et al.</i> (1963)
mucus viscosity	Pa s	μ_m	0.01	Erken <i>et al.</i> (2022)
air viscosity	Pa s	μ_a	1.8×10^{-5}	Dietze & Ruyer-Quil (2015)
mucus density	kg m^{-3}	ρ_m	1000	Erken <i>et al.</i> (2022)
air density	kg m^{-3}	ρ_a	1.2	Dietze & Ruyer-Quil (2015)
interfacial tension	N m^{-1}	γ	0.05	Erken <i>et al.</i> (2022)
airflow-driving force amplitude	N m^{-3}	A	18	chosen to match typical flow rates: Pedley (1977)
velocity scale	m s^{-1}	U	AR^2/μ_a	
respiratory frequency	Hz	$f_b U/R$	1	Pedley (1977)
mean/net cilia velocity	$\mu\text{m s}^{-1}$	$\langle u_c \rangle U$	40	chosen to match typical transport rates:(Choudhury <i>et al.</i> 2023)
cilia forward to reverse stroke ratio	[-]	a_f/a_r	2	Vasquez <i>et al.</i> (2016)
cilia-beat frequency	Hz	$f_c U/R$	10	Oldenburg <i>et al.</i> (2012)
metachronal wavelength	mm	$\lambda_c R$	40×10^{-3}	Blake (1975)
Reynolds number of air	[-]	Re_a	4	
Reynolds number of mucus	[-]	Re_m	6.1	
Capillary number	[-]	Ca	32	
viscosity ratio	[-]	Π_μ	1.8×10^{-3}	
density ratio	[-]	Π_ρ	1×10^{-3}	
initial film thickness	mm	$(1 - d_0)R$	0.008 - 0.045	
fastest-growing Rayleigh-Plateau wavelength	mm	Λ_{RP}	3.1 - 3.4	Rayleigh (1892)
computational domain length	mm	L	Λ_{RP}	

TABLE 2. Values of the parameters in the flow model, corresponding to the results in the main text. Some key figures are also produced for a second set of mucus-air properties in the [supplementary material](#).

$d(z, t)$ evolves without changing the total volume of mucus, which remains at its initial value of $(1 - d_0^2)LR^2$, where d_0 is the dimensionless position of the initially-flat film ($d(z, 0) = d_0$) and L is the length of the domain (see figure 1).

Equations (2.1), (2.2), (2.4) - (2.9), along with either (2.10) and (2.11), or just (2.12), form a closed system of equations. Most of the parameters are set to physiologically relevant values, listed in table 2. The initial film thickness, $1 - d_0$, is varied to study the effect of the mucus volume fraction.

2.2. Weighted-residual approach

We now average across the radial direction, using the WRIBL method, to obtain evolutions equations for the interface profile $d(z, t)$ and the flow rates of air and mucus, $Q_i(z, t)$. The derivation is outlined, in brief, in this section; for details, the reader is referred to Dietze & Ruyer-Quil (2015), whom we follow closely.

2.2.1. Velocity decomposition

The velocity field is decomposed into a leading-order contribution \hat{u}_i and a correction u'_i that is $O(\epsilon)$. The leading term accounts for the local balance between the $O(1)$ radial viscous diffusion and axial pressure gradients, while yielding the exact flow rate $2\pi Q_i$. Thus, \hat{u}_i is a self-similar radial profile that is parameterized by the cilia velocity, the flow rate, and the film thickness:

$$u_i(r, z, t) = \hat{u}_i(r; u_c, d, Q_i) + u'_i(r, z, t), \quad (2.13)$$

with

$$\frac{1}{r} \partial_r (r \partial_r \hat{u}_m) = A_m, \quad \frac{1}{r} \partial_r (r \partial_r \hat{u}_a) = A_a, \quad (2.14)$$

and

$$\hat{u}_m = u_c(z, t), \quad \hat{v}_m = 0 \quad \text{at } r = 1, \quad (2.15)$$

$$\partial_r \hat{u}_a = 0, \quad \hat{v}_a = 0 \quad \text{at } r = 0, \quad (2.16)$$

$$\partial_r \hat{u}_m = \Pi_\mu \partial_r \hat{u}_a, \quad \hat{u}_a = \hat{u}_m \quad \text{at } r = d, \quad (2.17)$$

where A_m and A_a are determined by the flow rates $2\pi Q_i$:

$$\int_0^d \hat{u}_a r dr = Q_a, \quad \int_d^1 \hat{u}_m r dr = Q_m. \quad (2.18)$$

Once d and Q_i are obtained by solving the WRIBL equations, given in the next sub-section, then \hat{u}_i can be calculated to obtain the leading axial velocity profile at any position in the airway. Furthermore, the leading radial-velocity profile can be obtained by integrating the continuity equation (2.1):

$$\hat{v}_a = -\frac{1}{r} \int_0^r \partial_z \hat{u}_a r dr, \quad \hat{v}_m = \frac{1}{r} \int_r^1 \partial_z \hat{u}_m r dr \quad (2.19)$$

In this manner, the leading-order, incompressible velocity field (\hat{u}_i, \hat{v}_i) is obtained. It is used to (i) evolve particles in the air-phase, and (ii) visualize the flow by plotting streamlines obtained from contours of the streamfunction Ψ_i :

$$\Psi_m = \int_r^1 \hat{u}_m r dr, \quad \Psi_a = \int_0^r \hat{u}_a r dr \quad (2.20)$$

Regarding the velocity corrections u'_i , equation (2.18) implies that they must satisfy the following gauge conditions, which will be used to eliminate u'_i from the weighted-averaged equations.

$$\int_0^d u'_a r dr = 0, \quad \int_d^1 u'_m r dr = 0 \quad (2.21)$$

2.2.2. Weighted-residuals

Denoting the boundary layer equations for the two phases in (2.2) by BLE_i , we obtain averaged equations by evaluating the residual $\langle BLE|w \rangle$ where the inner product is defined as $\langle p|q \rangle = \Pi_\mu \int_0^d p_a q_a r dr + \int_d^1 p_m q_m r dr$ and w_i are weight functions. If naive radial averaging is performed with $w_i = 1$, then the velocity correction u'_i will arise in the residual via the leading-order, radial viscous diffusion term. One will then have to either calculate u'_i or suffer prominent errors that can produce unphysical solutions (Kalliadasis *et al.* 2012). The ingenuity of the WRIBL approach (Kalliadasis *et al.* 2012; Dietze & Ruyer-Quil 2013) is to use a weight function which eliminates the correction from the residual (to $O(\epsilon^2)$).

Multiple choices for the weights are possible. We follow Dietze & Ruyer-Quil (2013, 2015)

and use two combinations. First, we choose w_i so that the pressure-gradient term is cancelled out and an evolution equation for Q_i is obtained. The defining equations for this weight function are

$$\frac{1}{r} \partial_r (r \partial_r w_m) = 1, \quad \frac{1}{r} \partial_r (r \partial_r w_a) = C_a, \quad (2.22)$$

with the homogeneous version of the \hat{u}_i boundary conditions:

$$w_m|_{r=1} = 0, \quad \partial_r w_a|_{r=0} = 0, \quad \partial_r w_m|_{r=d} = \Pi_\mu \partial_r w_a|_{r=d}, \quad w_a|_{r=d} = w_m|_{r=d}. \quad (2.23)$$

C_a in (2.22) follows from applying

$$\int_0^d w_a r dr = - \int_d^1 w_m r dr \quad (2.24)$$

The second weight function, denoted by \tilde{w}_i , is chosen to yield a diagnostic equation for the pressure at the interface, $p_i|_d$. This equation will be used to enforce axial pressure boundary conditions. The defining equations for \tilde{w}_i are

$$\frac{1}{r} \partial_r (r \partial_r \tilde{w}_m) = 1, \quad \frac{1}{r} \partial_r (r \partial_r \tilde{w}_a) = \tilde{C}_a, \quad (2.25)$$

with the same boundary conditions as w_i but with

$$\int_0^d \tilde{w}_a r dr = \int_d^1 \tilde{w}_m r dr, \quad (2.26)$$

instead of (2.24).

On applying the velocity decomposition (2.13), along with (2.21), the corrections u'_i cancel out from the residual $\langle BLE|w \rangle$ at $O(\epsilon^2)$, provided we neglect $O(Re_i \epsilon^2)$ inertial terms, as is appropriate for low to moderate Reynolds numbers (Dietze & Ruyer-Quil 2015).

Note that our choice of weight functions differs from that in Dietze & Ruyer-Quil (2015). Hence, the final WRIBL equations, listed below, have the same terms as those in Dietze & Ruyer-Quil (2015) but with different coefficients. We have checked that the predictions of our WRIBL equations match those of Dietze & Ruyer-Quil (2015), as illustrated by figure 15 in Appendix A.

2.2.3. WRIBL equations

Two exact mass-conservation equations follow from integrating the continuity equation (2.1) in the radial direction, in each phase, and using the kinematic boundary condition (2.8):

$$d \partial_t d = \partial_z Q_m, \quad (2.27)$$

$$\partial_z Q_m + \partial_z Q_a = 0 \quad (2.28)$$

where, alternately, the latter could be replaced by $d \partial_t d = -\partial_z Q_a$.

The evolution equation for the flow rate follows from evaluating the weighted-residual with respect to w_i :

$$\begin{aligned} & \frac{\mu_i}{\mu_m} Re_i \left(S_{ij} \partial_t Q_j + S_{ic} \partial_t u_c + F_{ijk} Q_j \partial_z Q_k + F_{ijc} Q_j \partial_z u_c + F_{icj} u_c \partial_z Q_j + F_{icc} u_c \partial_z u_c \right. \\ & \quad \left. + G_{ijk} Q_j Q_k \partial_z d + G_{icj} u_c Q_j \partial_z d + G_{icc} u_c u_c \partial_z d \right) \\ & = -C_a (\partial_z \kappa + \partial_z \kappa_p) I w_a + \Pi_\mu C_a Q_a + Q_m + J_j Q_j (\partial_z d)^2 + J_c u_c (\partial_z d)^2 \\ & \quad + K_j \partial_z Q_j \partial_z d + K_c \partial_z u_c \partial_z d + L_j Q_j \partial_z^2 d + L_c u_c \partial_z^2 d \\ & \quad + M_j \partial_z^2 Q_j + M_c \partial_z^2 u_c - u_c \partial_r w_m|_1 + \Pi_\mu G_a \sin(\omega t) I w_a, \quad (2.29) \end{aligned}$$

where Einstein summation notation has been used on the phase index. The coefficients, $S_{ij}, S_{ic}, F_{ijk}, \dots, M_c$ are functions of d alone. The integrals of \hat{u} and w_i , which yield these coefficients, are involved and the corresponding calculations are performed using the Python symbolic-computing library SymPy (Meurer *et al.* 2017).

Note that, for convenience of notation, we have written the WRIBL equation (2.29) after rescaling the axial coordinate with R ; thus the length-scale ratio ϵ does not appear here. This new axial scaling will be used to present all subsequent equations and figures.

Equations (2.27) to (2.29) form a closed system for d , Q_m and Q_a . Integrating (2.28) shows that the total flow rate, $Q_t(t) = Q_a + Q_m$, is spatially invariant. Therefore, given Q_t as an input, one can replace Q_a by $Q_t - Q_m$ and solve (2.27) and (2.29) for d and Q_m . Here, however, we do not impose Q_t . Rather, we impose the background pressure-gradient, so that the net pressure difference across the computational domain, of length L , must be $G_a L \sin(\omega t)$ in the air and zero in the mucus. The deviation from this applied pressure-gradient, p_i , must therefore integrate to zero over the domain:

$$\int_0^{L/R} \partial_z p_i dz = 0 \quad (2.30)$$

To apply this pressure constraint, we require the diagnostic equation for pressure, which is obtained by evaluating the weighted-residue with respect to \tilde{w}_i :

$$\begin{aligned} & \frac{\mu_i}{\mu_m} Re_i \left(\tilde{S}_{ij} \partial_t Q_j + \tilde{S}_{ic} \partial_t u_c + \tilde{F}_{ijk} Q_j \partial_z Q_k + \tilde{F}_{ijc} Q_j \partial_z u_c + \tilde{F}_{icj} u_c \partial_z Q_j + \tilde{F}_{icc} u_c \partial_z u_c \right. \\ & \quad \left. + \tilde{G}_{ijk} Q_j Q_k \partial_z d + \tilde{G}_{icj} u_c Q_j \partial_z d + \tilde{G}_{icc} u_c u_c \partial_z d \right) \\ & = -2\Pi_\mu \partial_z p_a|_d \tilde{I}w_a + Ca (\partial_z \kappa + \partial_z \kappa_p) \tilde{I}w_a + \Pi_\mu \tilde{C}_a Q_a + Q_m + \tilde{J}_j Q_j (\partial_z d)^2 + \tilde{J}_c u_c (\partial_z d)^2 \\ & \quad + \tilde{K}_j \partial_z Q_j \partial_z d + \tilde{K}_c \partial_z u_c \partial_z d + \tilde{L}_j Q_j \partial_z^2 d + \tilde{L}_c u_c \partial_z^2 d \\ & \quad + \tilde{M}_j \partial_z^2 Q_j + \tilde{M}_c \partial_z^2 u_c - u_c \partial_r \tilde{w}_m|_1 + \Pi_\mu G_a \sin(\omega t) \tilde{I}w_a. \quad (2.31) \end{aligned}$$

As is customary when using thin-film models to describe droplets, rivulets, and other situations involving regions devoid of liquid (Oron *et al.* 1997; Ghatak *et al.* 1999; Ruyer-Quil *et al.* 2023), we employ a precursor-film approach to capture the mucus-depleted zones of the airway. To wit, we introduce a disjoining pressure via the term $\kappa_p = \frac{h_0^6}{(1-d)^9}$ in (2.29) and (2.31). With $h_0 = 5 \times 10^{-4}$, we obtain a precursor film thickness below 0.01 ($d > 0.99$) in the depleted zones; the fluid drained out of these zones accumulates in annular humps whose shape, we have verified, is very close to that of equilibrium unduloids (of the same volume). Reducing the precursor film's thickness even further does not affect our results but significantly increases the computational cost.

The coefficients of (2.29) and (2.31) are stored in text files and imported when performing numerical simulations, as done in the Jupyter notebook associated with figure 15 in Appendix A.

2.2.4. One-way coupled WRIBL equations

Given that air has a much smaller viscosity and density than mucus, it is natural to check whether the simplified model obtained in the limit of $\Pi_\rho, \Pi_\mu \ll 1$ provides a good approximation of the two-phase flow. In this limit, the mucus film evolves independently of the air, with a stress-free surface. Such a passive-core approximation is routinely made when studying gas-liquid flows in which the gas flow is weak. While this approximation is certainly inappropriate for the upper airways, where the turbulent airflow is strong enough to rip off mucus droplets from the film, it could work well in the middle airways where the airflow is much weaker.

The WRIBL model for the mucus phase in the passive-core limit was analysed by Dietze &

Ruyer-Quil (2015). Here, we additionally derive the WRIBL equation for the air phase, because we need the air velocity field in order to study aerosol transport. In the limit of infinite viscosity contrast, the air will experience the mucus film as a moving solid boundary. Thus, while the mucus film evolves independently, the airflow is modulated by the deformation of the film, *i.e.*, we have a one-way coupled flow. Because the mucus velocity is typically much slower than that of the air, the major effect of the film is to alter the conduit for airflow.

The decoupled mucus flow is governed by the domain equations (2.1) and (2.2), with $i = m$, the wall boundary-condition (2.10), the kinematic condition (2.8), and the free surface conditions obtained by setting $\Pi_\mu = 0$ in (2.5) and (2.6). (The smallness of Π_ρ is used implicitly when we set $\Pi_\mu p_a$ to zero, in (2.6); Π_ρ controls the relative strength of air pressure variations, in cases where inertia is significant.) We then apply the WRIBL method to the mucus phase by performing the weighted integral from $r = d$ to $r = 1$. The leading-order mucus velocity is determined by the equations for \hat{u}_m in (2.14) to (2.18) but now with $\Pi_\mu = 0$. Similarly, the weight function is defined by the equations for w_m in (2.22) and (2.23), with $\Pi_\mu = 0$. The resulting WRIBL model for the mucus-film is as follows:

$$d\partial_t d = \partial_z Q_m \quad (2.32)$$

$$\begin{aligned} Re_m \left(\bar{S}_{mm} \partial_t Q_m + \bar{S}_{mc} \partial_t u_c + \bar{F}_{mmm} Q_m \partial_z Q_m + \bar{F}_{mmc} Q_m \partial_z u_c + \bar{F}_{mcc} u_c \partial_z u_c + \right. \\ \left. \bar{F}_{mcm} u_c \partial_z Q_m + \bar{G}_{mmm} Q_m Q_m \partial_z d + \bar{G}_{mcm} Q_m u_c \partial_z d + \bar{G}_{mcc} u_c u_c \partial_z d \right) \\ = Ca (\partial_z \kappa + \partial_z \kappa_p) \bar{I} w_m + Q_m + \bar{J}_m Q_m (\partial_z d)^2 + \bar{J}_c u_c (\partial_z d)^2 + \bar{K}_m \partial_z Q_m \partial_z d \\ + \bar{K}_c \partial_z u_c \partial_z d + \bar{L}_m Q_m \partial_z^2 d + \bar{L}_w u_c \partial_z^2 d + \bar{M}_m \partial_z^2 Q_m + \bar{M}_c \partial_z^2 u_c - u_c \partial_r \bar{w}_m|_1 \quad (2.33) \end{aligned}$$

Equations (2.32) and (2.33) must be solved simultaneously to determine Q_m and d , which will then be used as inputs to calculate Q_a from the WRIBL equation in the air phase. The leading-order air velocity \hat{u}_a is determined by (2.14) and (2.18) along with the boundary conditions $\partial_r \hat{u}_a|_0 = 0$ and $\hat{u}_a|_d = \hat{u}_m|_d$. The weight function w_a satisfies the homogeneous version of these boundary conditions, in addition to (2.22). Performing the weighted integral over the air phase, from $r = 0$ to $r = d$, yields the WRIBL equation for the airflow:

$$\begin{aligned} Re_a \left(\bar{S}_{aa} \partial_t Q_a + \bar{S}_{ad} \partial_t u_d + \bar{F}_{aaa} Q_a \partial_z Q_a + \bar{F}_{aad} Q_a \partial_z u_d + \right. \\ \left. \bar{F}_{ada} u_d \partial_z Q_a + \bar{F}_{add} u_d \partial_z u_d + \bar{G}_{aaa} Q_a Q_a \partial_z d + \bar{G}_{ada} u_d Q_a \partial_z d + \bar{G}_{add} u_d u_d \partial_z d \right) \\ = -\partial_z p_a|_d \bar{I} w_a + \bar{C}_a Q_a + \bar{J}_a Q_a (\partial_z d)^2 + \bar{J}_d u_d (\partial_z d)^2 + \bar{K}_a \partial_z Q_a \partial_z d + \bar{K}_d \partial_z u_d \partial_z d \\ + \bar{L}_a Q_a \partial_z^2 d + \bar{L}_d u_d \partial_z^2 d + \bar{M}_a \partial_z^2 Q_a + \bar{M}_d \partial_z^2 u_d + G_a \sin(\omega t) \bar{I} w_a - u_d \partial_r \bar{w}_a|_d. \quad (2.34) \end{aligned}$$

This equation, which has the air flow rate Q_a and the pressure at the interface $p_a|_d$ as unknowns, must be solved along with the overall mass balance equation (2.28).

2.2.5. Numerical solution

To solve the fully coupled WRIBL equations, we first use (2.28) to substitute $Q_m = Q_t(t) - Q_a$ in (2.29) and (2.31). The latter pressure-equation is then integrated over the domain and the pressure-constraint (2.30) is applied to obtain an ordinary differential equation (ODE) for $Q_t(t)$ of the form

$$d_t Q_t = \Phi(d, Q_a, Q_t, u_c) \quad (2.35)$$

Equations (2.27), (2.29) and (2.35) thus become a closed system for d , Q_a and Q_t .

Numerical simulations are performed by discretizing space using a second-order central-difference scheme. The resulting system of ODEs is integrated in time using the stiff, adaptive time-stepping, LSODA solver (Hindmarsh & Petzold 1995) provided by the function `solve_ivp`, of the Python library SciPy (Virtanen *et al.* 2020).

Turning to the one-way coupled WRIBL model, the equations for the mucus film, namely (2.32) and (2.33), are solved first to obtain d and Q_m . Here too we employ second-order central-differencing in space, followed by the LSODA method for stepping in time. To obtain Q_a , we need only solve for Q_t , since $Q_a = Q_t(t) - Q_m$; on substituting this relation into the one-way coupled WRIBL equation for air, (2.34), integrating over the domain, and applying the pressure constraint (2.30), we obtain an ODE for Q_t . So, rather than simultaneously solving two partial differential equations (PDEs) and one ODE, as required by the fully coupled WRIBL model, we solve just two PDEs first and then separately solve a single ODE.

All our simulations are performed with periodic boundary conditions in the axial z direction. The length of the computational domain L is chosen to match the wavelength of the fastest growing mode of the Rayleigh-Plateau instability, $\Lambda_{RP} = 2\pi^{1/2}d_0R$. (This inviscid prediction of Rayleigh (1892) works very well even for viscous films (Dietze & Ruyer-Quil 2015).) An evenly-spaced spatial grid of 500 points is found to be sufficient for obtaining grid-independent solutions.

2.3. Particle motion

To track the motion of airborne particles, we adopt the point-particle approximation and use the Maxey-Riley equation, simplified for tiny dense particles (Ravichandran *et al.* 2017). In addition, we include Brownian forces, in order to describe a wide range of particles, from Brownian to inertial. The particle's position \mathbf{X}_p and velocity \mathbf{V}_p are thus governed by the following stochastic differential equations (SDEs), which are often used for studying particle transport in the lungs (Tsuda *et al.* 2013):

$$d\mathbf{X}_p = \mathbf{V}_p dt \quad (2.36)$$

$$St d\mathbf{V}_p = \mathbf{u}(\mathbf{X}_p, t)dt + \sqrt{\frac{2}{Pe}} d\mathbf{W}, \quad (2.37)$$

where \mathbf{u} is the air-velocity vector which must be obtained at the instantaneous position of the particle, \mathbf{X}_p . Brownian forces are modelled by $d\mathbf{W}$, a vector of independent increments of the Wiener process (Gardiner 2009). The impact of Brownian forces on the particle's motion varies inversely with the Péclet number (Pe), which is the ratio of the timescales of Brownian diffusion to convection by the airflow. The importance of inertial effects increases with the Stokes number (St), which is the ratio of the timescale of the particle's inertial relaxation to the time-scale over which the flow changes (as viewed by the convected particle). In our study, Pe and St are not independent but vary together with the particle diameter d_p , as follows:

$$Pe = \frac{RU_{\max}}{D} \text{ with } D = \frac{k_B T}{3\pi\mu_a d_p}, \text{ and } St = \frac{d_p^2 \rho_p U_{\max}}{18\mu_a R}, \quad (2.38)$$

where D is the Einstein diffusivity of the particle, k_B is the Boltzmann constant, $T = 298K$ is the temperature, and ρ_p is the particle's density. $U_{\max} = \max_t [\langle u_a |_{d_{\min}} \rangle_r] U$ is the maximum, over time, of the cross-section averaged air velocity below the mucus hump (the z location where $d = d_{\min}$); it yields an estimate of the smallest convective time-scale during respiration. We fix the particle's density to that of water ($\rho_p = 1000 \text{ kg m}^{-3}$) and vary the diameter from 10^{-3} to $50 \mu\text{m}$. Both Pe and St increase strongly with d_p (see table 3) so that the motion of the smallest particles is nearly Brownian while that of the largest is influenced by inertial effects, such as

Parameter	Symbol	Minimum	Maximum
diameter (μm)	d_p	0.001	50
diffusion time (s)	–	6.39	3.2×10^5
Péclet number	Pe	1×10^2	9×10^6
inertial relaxation time (s)	–	3×10^{-12}	7×10^{-3}
Stokes number	St	9×10^{-11}	2×10^{-1}

TABLE 3. Range of particle sizes considered in this study and the corresponding timescales and non-dimensional numbers.

migration across curved streamlines. Intermediate-sized particles are affected the least by these forces and tend to follow the flow like tracers.

In solving (2.36)-(2.37), we use a two-step exponential integration scheme, which enables accurate simulations of small St particles (Ireland *et al.* 2013). The Wiener increment dW is updated only once every time step (it stays the same for both half-steps); thus, the Brownian term is integrated using the Euler-Marujama scheme (Öttinger 1996). This strategy, of using higher-order time-stepping for the drift terms of an SDE, is helpful when the relative importance of Brownian forces varies widely; it has been used, for example, to study Brownian elastic chains in turbulent flows (Bagheri *et al.* 2012; Singh, Picardo & Ray 2012).

The solution of the WRIBL model yields the air velocity field in axisymmetric cylindrical coordinates. We transform this field to three-dimensional Cartesian coordinates and then evolve particles in three-dimensions. The air velocity at the particle location is obtained from its value on the computational grid via linear interpolation. We consider the dilute limit and neglect inter-particle collisions. Thus, the motion of each particle is independent of all others in the airway; we use this fact to parallelize the numerical integration of the particles to accelerate simulations. We track up to 2000 particles in a given flow, for up to 30 breathing cycles.

Adopting the simplest approach to studying deposition, we assume that a particle deposits when its surface makes contact with the film (Guha 2008). We therefore monitor the radial distance (along the r coordinate of the airway) between the centre of mass of the particle and the mucus-air interface; if this distance falls below $d_p/2$, then we assume that the particle has collided with the mucus film and become instantly entrapped; the trapped particle is no longer evolved. Strictly speaking, we should monitor the shortest distance between the particle and the interface, but this would be computationally expensive. So, noting that axial variations of the film occur over distances much larger than the particle’s radius, we replace the shortest distance by the radial distance. In keeping with our use of a precursor film to represent mucus-depleted sections of the wall, we treat all particles that collide with the precursor film (of thickness less than $0.01R$) as having deposited on the wall.

This model of particle transport, while simple, captures the key physical aspects of deposition in a mucus-lined airway: (i) size-dependent Brownian and inertial forces, (ii) possibility of deposition on mucus-depleted zones of the wall, and (iii) influence of spatially non-uniform airflow, due to the presence of protruding mucus humps. There are of course various directions in which the particle model can be improved. In particular, the largest particles considered here are $1/8$ times the diameter of the airway and are thus not well-suited to be treated as point particles. Nonetheless, we include these particles in our study, with the aim of providing a first approximation to their deposition behaviour. Indeed, the influence of finite-size effects (such as shear-gradient-induced lift and wall-induced lift) on the particle’s motion scale with the fluid to particle density ratio (Guha 2008; Liu *et al.* 2016); here $\rho_p/\rho_a = 10^{-3}$ and so the effects of finite-size will be weak in

comparison to the effects of particle inertia (such as centrifugation). The latter will be shown to play an important role in the presence of a non-uniform mucus film.

3. How cilia and air affect the mucus film

We shall first examine how the mucus film—its distribution and flow—is affected by cilia and air. Then, in § 4, we will quantify the extent of mucus depleted zones. The understanding of the flow gained in these sections will aid our study of particle deposition, which will be taken up in § 5.

All our simulations use the parameters given in table 2, which are typical for mucus and air in a middle airway (we focus on generations 14-16). Our results are not sensitive to the precise values of the parameters, as demonstrated in the [supplementary material](#) which reproduces select figures for a different value of the viscosity ratio and interfacial tension.

Throughout this work, we set the length of the computational domain to match the wavelength of the fastest growing mode of the Rayleigh-Plateau instability, i.e., $L = \Lambda_{RP} = 2\pi 2^{1/2} d_0 R$ (Rayleigh 1892; Dietze & Ruyer-Quil 2015). Furthermore, we only consider films with an initial thickness $1 - d_0$ sufficiently small to remain open without forming a liquid bridge, i.e., with $(1 - d_0^2)\Lambda_{RP}/R < 1.73$ (Dietze & Ruyer-Quil 2015; Everett & Haynes 1972). In the present section, representative results for the air-mucus flow are shown for the value of $d_0 = 0.885$. The simulations are initialized with a slightly perturbed interface, $d = d_0 + 10^{-3} \cos(2\pi z R / \Lambda_{RP})$. Random perturbations will be applied later, in § 4, while analysing the extent of mucus-depleted zones.

3.1. Cilia translates the mucus film

The effect of cilia on the film profile is illustrated in figure 2. Snapshots of the evolution of the interface with ciliary forcing (via the metachronal velocity u_c imposed at the wall, as per (2.11)) are compared with those without ciliary forcing (setting $u_c = 0$), in panels (a-c) and (d-f). The same unduloid-shaped hump is formed in both cases, but the hump translates in the presence of cilia. The growth of the hump, visualized by the time trace of the minimum position of the interface in figure 2(g), is indeed nearly identical in the two cases. In this and all subsequent plots, we present the temporal evolution in multiples of the non-dimensional breathing time-period T_b (where the dimensional time period, $T_b R / U$ is 1 s).

The cilia-induced translation shows up clearly in figure 2(h) which traces the location of the centre-of-mass of the film, X_{cm} ; the translation is near-linear with a constant speed equal to the mean cilia speed $\langle u_c \rangle$. When this linear translation is subtracted out, as done in the inset, we find that tiny oscillations are superimposed on the linear translation; the oscillations are caused by respiratory airflow as evidenced by their presence in the case without cilia (for which we use $\langle u_c \rangle = 0$ in the inset).

These air-induced oscillations are also seen in the root-mean-square averaged velocity of mucus, $\langle u_m \rangle_{\text{rms}} = [\int_0^L u_m^2 dz]^{1/2}$, which is plotted in figure 2(i). Here, the prominent peak in $\langle u_m \rangle_{\text{rms}}$ corresponds to the relatively rapid capillary-driven flow of mucus that produces the hump. After the hump has formed (and the capillary forces due to axial and radial curvatures have balanced out) the interface profile remains unchanged while the cilia slowly transports the film.

Since hump-formation is a one-time event, we will focus on the long term motion of the film for our study of particle deposition. The space-time kymograph of the interface profile in figure 3(a) emphasizes that this long-term motion is dominated by simple translation. In fact, if we replace the asymmetric metachronal wave form of u_c in (2.11) by just its mean, as given by the constant velocity Couette condition in (2.12), we obtain a near-identical translatory motion of the interface, as shown in figure 3(c). The streamlines in the air and mucus phases are also found

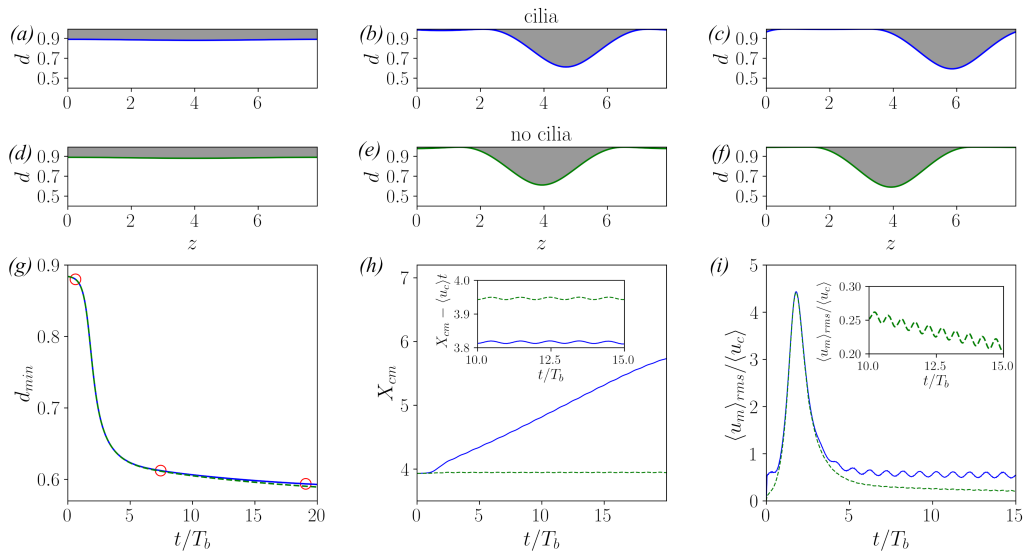


FIG. 2. Cilia translates the mucus film without altering the capillary-driven dynamics and the consequent emergence of humps and depleted zones. The top two rows present snapshots of the evolution of the film, with cilia (*a-c*) and without cilia, *i.e.*, with $u_c = 0$ (*d-f*). Panel (*g*) compares the growth of the hump by tracing the evolution of the minimum of $d(z, t)$. Panel (*h*) compares the time-traces of the centre of mass of the entire film, clearly showing that cilia causes the film to translate; the inset subtracts out the net translation $\langle u_c \rangle t$ and reveals tiny lateral air-induced oscillations. Panel (*i*) presents the time-trace of the spatially-averaged root-mean-square mucus velocity, normalized with the mean cilia velocity; the inset zooms into the curve for the no-cilia case.

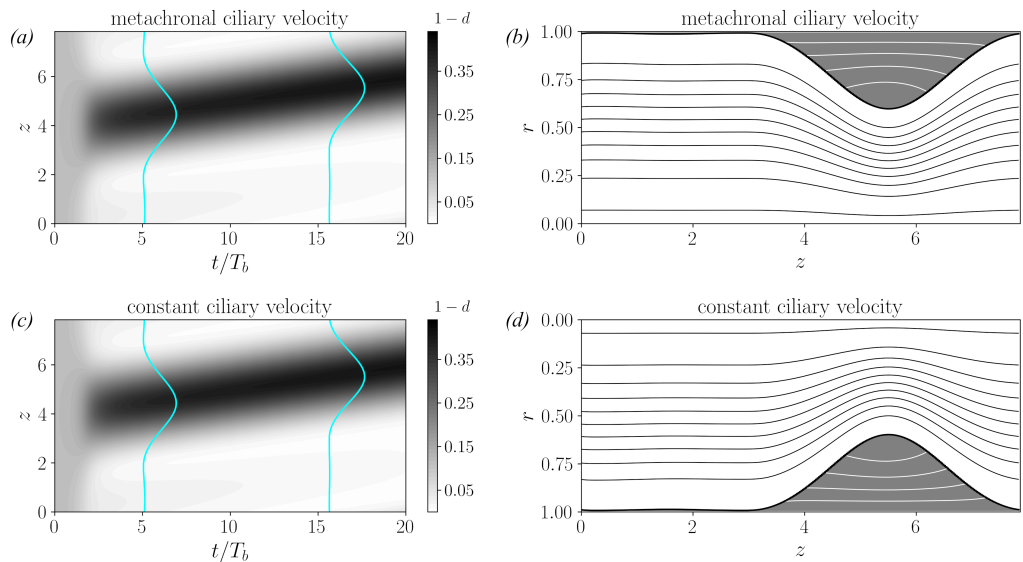


FIG. 3. The metachronal cilia velocity (2.11) has the same effect on the flow as the constant cilia velocity (2.12), as evidenced by the kymographs of the evolution of the film thickness $1 - d(z, t)$ (panels *a, c*) and the snapshots of the streamlines in the air and mucus (panels *b, d*). The snapshot of the streamlines corresponds to the time of the second line profile drawn in the kymographs ($t \approx 15.6 T_b$).

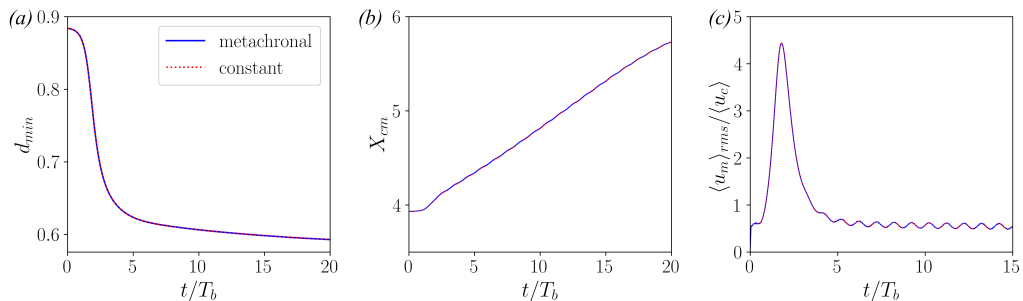


FIG. 4. Comparison of the time traces of (a) the minimum position of the interface, (b) the centre-of-mass of the film, and (c) the root-mean-square mucus velocity, for the metachronal and constant cilia velocities (given by (2.11) and (2.12) respectively). The curves overlap in each panel showing perfect agreement.

to match very well (compare figures 3*b* and 3*d*). Further evidence for this equivalence is provided in figure 4 in which the time-traces of d_{min} , X_{cm} , and $\langle u_m \rangle_{rms}$ for the constant cilia velocity are seen to match those for the metachronal cilia velocity. Thus, the metachronal waveform of u_c plays no role in the evolution of the interface and the net mucociliary transport—only the mean $\langle u_c \rangle$ matters (we have checked that this result is independent of spatial resolution by increasing the grid points from 300 to 1024). Hence, in all subsequent results, we shall use the constant cilia velocity boundary condition (2.12), both for simplicity and ease of computation (without the relatively rapid oscillations in u_c we can take much larger time steps while integrating the WRIBL equations).

Of course, our conclusion regarding the unimportance of the metachronal waveform is valid only for the slow evolution of the film over long times scales; indeed, this result is unsurprising given that the cilia-beating time period is about three orders of magnitude smaller than the time scale with which mucus is transported across the airway (table 1). Another caveat is that we have considered a Newtonian mucus film, in which the dominant mechanism of momentum transport from the ciliary boundary is viscous diffusion, which effectively filters out the rapid oscillations of u_c . In contrast, for strongly viscoelastic mucus, present under diseased conditions, Choudhury *et al.* (2023) have shown that the metachronal waveform of u_c produces a substantial reduction of the net mucociliary transport (in a flat, non-deforming mucus film). However, for healthy mucus, which is not as viscoelastic, this effect is marginal; indeed, the flow rate of a flat Newtonian film is shown to depend only on $\langle u_c \rangle$ (Choudhury *et al.* 2023).

The cilia-induced translation of mucus is much slower than the respiratory airflow, as is evident in figure 2(*h*): the interface hardly moves in a single breath, *i.e.*, in a time interval of T_b (see also the corresponding time and velocity scales in table 1). So, the interface will appear to be stationary to air-borne particles which typically travel back and forth across the domain with each breath. Indeed, we see in figure 3(*b*) that the air streamlines bend around the mucus hump as if it were stationary. So, while ciliary transport of mucus is essential for the ultimate evacuation of trapped particles from the lungs, it cannot play a role in the deposition of particles on the mucus; mucociliary transport is simply too slow relative to the motion of airborne particles to produce any collisions that would not occur without cilia.

3.2. Airflow does not alter the distribution of the mucus film

Next, we consider the effect of respiratory airflow on the film. The small oscillations in figure 2(*i*) show that the flow of mucus is marginally modulated by the airflow. This effect would obviously not be captured by the one-way coupled WRIBL model, in which the flow of air does not affect that of mucus. However, aerosol transport and deposition depend crucially on the

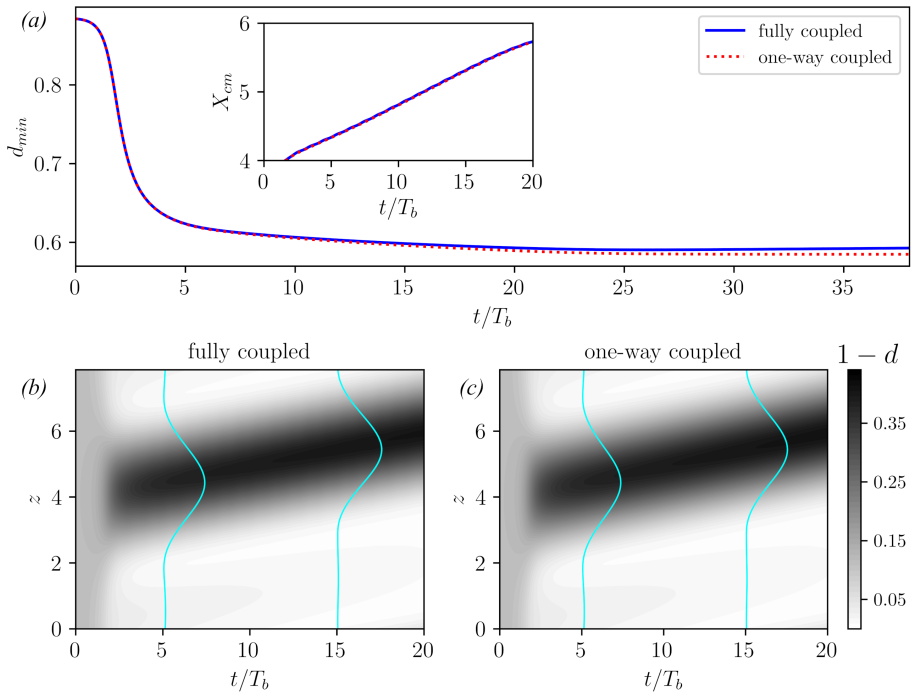


FIG. 5. Comparison of the interface evolution predicted by the fully-coupled and the one-way coupled WRIBL models; in the latter, air does not affect the flow mucus film. (a) Evolution of the minimum interface position (main panel) and the centre of mass (inset). Kymographs of the film thickness are compared in panels (b-c). ($t \approx 15T_b$).

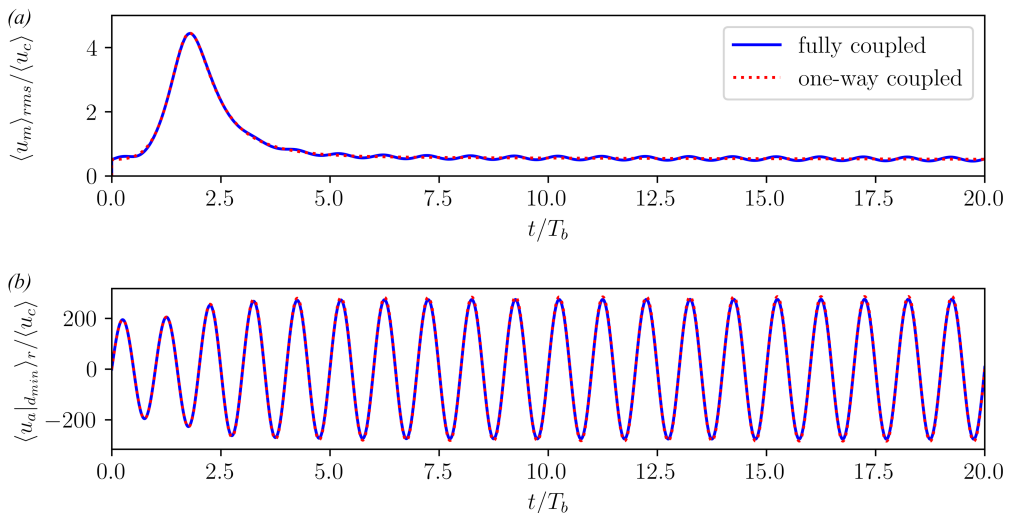


FIG. 6. Comparison of the evolution of averaged velocities in (a) mucus and (b) air, as predicted by the fully-coupled and the one-way coupled WRIBL models. Panel (a) presents the spatially-averaged root-mean-square mucus velocity; note the absence of the small air-induced oscillations in prediction of the one-way coupled model, which ignores the influence of air on the mucus film. Panel (b) presents the radial average of the air velocity just below the hump, i.e., below the thickest part of the interface given by d_{min} .

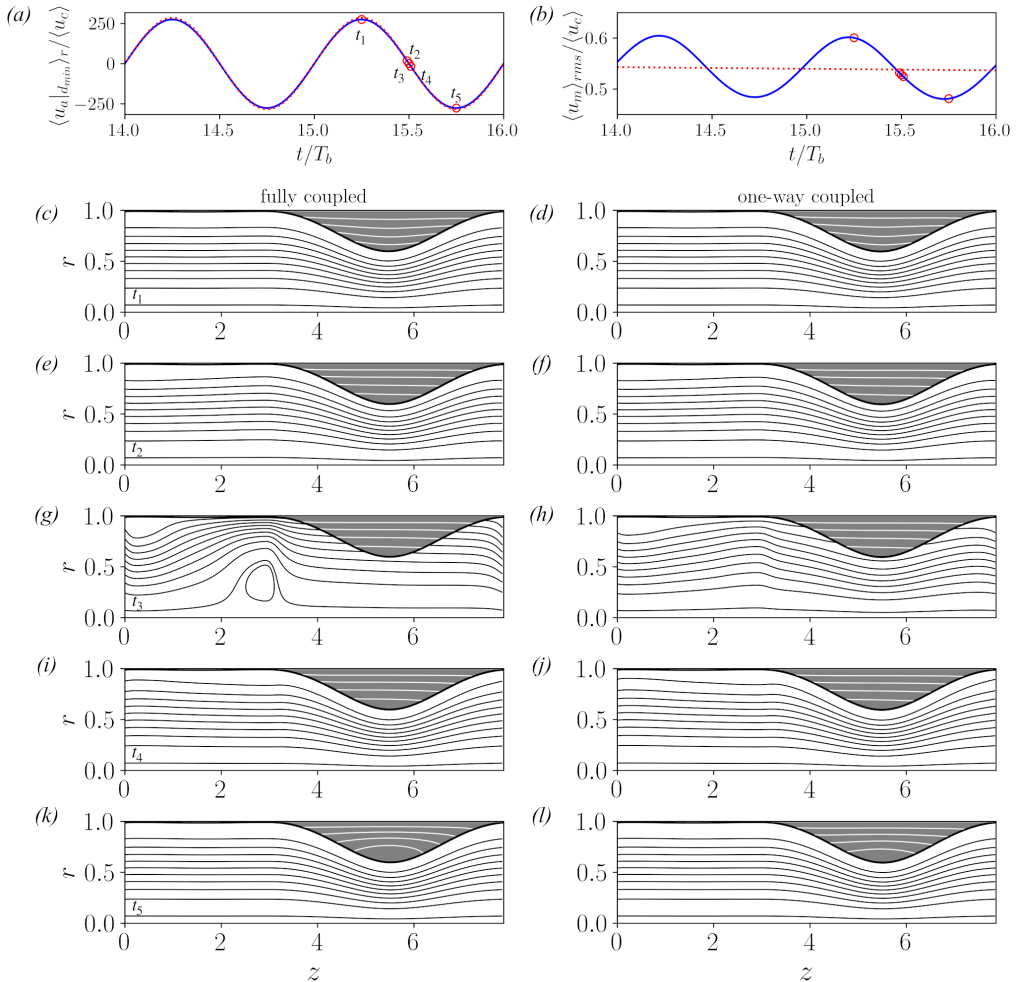


FIG. 7. Detailed comparison of the air and mucus flows predicted by the fully-coupled and one-way coupled WRIBL models; the latter ignores the influence of air on the mucus film. Panels (a) and (b) are temporal zooms of figures 6(b) and 6(a), respectively, showing the temporal variation of the mean air velocity (below the hump) and the mean mucus velocity. The line-legend is the same as that in figure 6. Five time-points are chosen, labelled t_1 to t_5 , corresponding to times when the airflow is opposite to cilia-transport (t_1), is in the same direction as cilia-transport (t_2), and is reversing ($t_3 - t_5$). The streamlines in the air and mucus at these five times are compared in panels (c-l) for the fully-coupled (left column, with inset time-labels) and one-way coupled (right column) models.

mucus film's distribution (shape and size of humps and depleted zones) and not on its internal flow. Moreover, because the flow of mucus is much slower than that of air, the film will influence the airflow primarily via changes in its profile. The interface profile $d(z, t)$, and the flow of air around it, might well be captured by the one-way model even though the flow inside the mucus film is not exactly reproduced.

Figure 5 shows that the one-way coupled model does indeed capture the evolution of the interface almost perfectly. The time traces of X_{cm} and the minimum of d practically overlap (figure 5a), and the kymographs exhibit the same translating hump (figures 5b-5c).

Is the airflow reproduced as accurately by the one-way coupled model? Figure 6 compares time traces of (a) the root-mean-square mucus velocity, and (b) the radially-averaged axial velocity

below the hump, obtained from the fully coupled and the one-way coupled models. We see that though the mucus flow is not entirely reproduced—the small air-induced oscillations are missing—the airflow does appear to be accurately predicted by the one-way coupled model.

Figure 7 compares the predictions of the airflow in more detail. Panels (a) and (b) zoom into a few oscillations of the long-term air and mucus flow. The remaining panels present snapshots of the instantaneous streamlines, for five selected time points within one breathing cycle, $t_1 - t_5$ in figure 7(a). Comparing the streamline plots in the left column (fully coupled model) with those on the right (one-way coupled model), we see that the air streamlines are perfectly captured by the one-way model except for the tiny duration of time between inhalation and exhalation when the airflow is reversing (see figures 7g and 7h corresponding to time t_3). For most of the breathing cycle, the airflow is orders of magnitude faster than the mucus flow (compare the y-axis ranges of figures 7a and 7b), and so the air flows past the mucus film as if it were a stationary solid wall. But, when the air velocity is reversing, its magnitude becomes comparable to that of the mucus velocity for a short period of time; this is when the flows in the two fluids are strongly coupled. However, the corresponding time duration is extremely small, as evidenced by the snapshots at times t_2 and t_4 just before and after t_3 (see figure 7a). At both these times, the air streamlines again flow around the mucus as if it were stationary, and the one-way coupled model captures the airflow very well (figures 7e and 7f for t_2 , 7i and 7j for t_4).

Thus, from the perspective of particle transport and deposition, the one-way coupled model is well-suited to describe the flow of air: Particles will hardly move during the time for which the airflow is inaccurately predicted by the one-way model, because not only is the corresponding time duration very small but also the airflow speed is nearly zero. We will therefore use the one-way coupled WRIBL model to obtain the interface profile and the air flow field for our analysis of particle transport in § 5.

4. Extent of mucus-depleted zones on the wall

We have seen, in the previous section, that the mucus film ultimately forms an unduloid-like hump that spans a portion of the wall, leaving the rest of the wall without mucus and exposed to particles (figure 2a-c). We now examine how the extent of these mucus-depleted zones varies on increasing the volume or, equivalently, the initial thickness $1 - d_0$ of the film.

We have performed numerous simulations of randomly-perturbed films, with different initial thicknesses ($1 - d_0$). For every value of d_0 , an ensemble of 8 independent simulations have been performed, starting from random initial perturbations to the flat film:

$$d(z, 0) = d_0 + 10^{-3} \sum_{m=1}^{10} A_m \cos(2\pi m z R / \Lambda_{RP} + \varphi_m), \quad (4.1)$$

where A_m and φ_m are uniformly distributed random numbers between $[0, 1]$ and $[0, 2\pi]$ respectively. Each simulation is run for a sufficiently long time so that the film attains its asymptotic profile. We use the one-way coupled WRIBL model (airflow does not affect the interface evolution, see § 3.2) and solve only the mucus-film equations (2.32)-(2.33), along with the constant cilia velocity boundary condition (2.12). Cilia transport, though, has no effect on the depleted zones because it does not alter the shape of the interface (see § 3.1). (We have checked that decreasing the cilia velocity by a factor of ten leaves the extent of depleted zones unchanged.)

In our simulations, the depleted zones are occupied by the precursor film. So, we measure the fraction of the wall occupied by depleted zones, D_f , by measuring the length of wall along which $1 - d < \delta$, where $\delta \approx 0.01$ is the thickness of the precursor film.

Our results are presented for a range of initial film thicknesses $1 - d_0$ in figure 8(a). Here, the markers and bars depict the mean and standard deviation of D_f obtained from the ensemble of

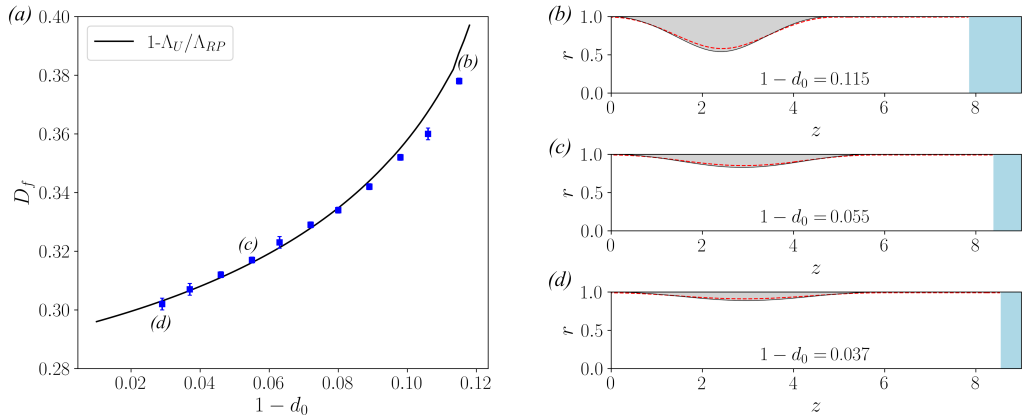


FIG. 8. (a) Fraction of the wall occupied by mucus-depleted zones. The prediction (4.2) is compared with measurements from randomly-initialized simulations. The markers and bars correspond to the mean and standard deviation of the values measured from the ensemble of eight simulations or each value of d_0 . (b-d) Shapes of unduloids (shaded in gray) for three values of the initial film thickness, overlaid with the final profile of the film (red-dashed line) from one of the runs in the corresponding ensemble of simulations. The same range of the axial z coordinate is used in these three panels for ease of comparison; the cyan-shaded padding is added to Λ_{RP}/R to achieve the same z -range.

simulations for each value of d_0 . Surprisingly, adding more mucus (increasing $1 - d_0$) does not decrease the extent of depleted zones but rather increases it and leaves more of the wall exposed to particles.

This counter-intuitive variation of D_f can be predicted by assuming that all the fluid contained in the initially flat film, of thickness $(1 - d_0)R$ and length Λ_{RP} (the domain length), is ultimately gathered into an equilibrium-shaped unduloid. This unduloid's axial width Λ_U will be less than Λ_{RP} (both of which depend on d_0), and the difference $\Lambda_{RP} - \Lambda_U$ will be the extent of the mucus-depleted zone. We thus obtain the following prediction for D_f :

$$D_f \approx 1 - \Lambda_U / \Lambda_{RP}. \quad (4.2)$$

Λ_{RP} , obtained from a linear stability analysis of the WRIBL model, is well approximated by the inviscid result of Rayleigh (1892), $\Lambda_{RP} = 2\pi 2^{1/2} d_0 R$ (Dietze & Ruyer-Quil 2015). To obtain Λ_U , we calculate the shape of the unduloid $g(z)$ that (i) has a constant mean-curvature and (ii) encloses the entire volume of the film:

$$\frac{1}{g} - \frac{(d_z g)^2}{2g} - d_{zz} g = K, \quad g(0) = 1, \quad d_z g|_0 = 0, \quad g(\Lambda_U/R) = 1,$$

$$2\pi \int_0^{\Lambda_U/R} \int_{g(z)}^1 r dr dz = \pi(1 - d_0^2) \Lambda_{RP}/R, \quad (4.3)$$

where K is a constant that is determined by the volume constraint. Note that we have used the $\mathcal{O}(\epsilon^2)$ expression (2.7) for the mean curvature to be consistent with the WRIBL model. We solve (4.3) numerically using a shooting method: We start with a value for K and solve an initial value problem for g , stepping forward in z until we satisfy the end boundary condition $g = 1$; we thus obtain the unduloid length Λ_U , after which the unduloid's volume can be calculated. By varying K , we obtain unduloids of all volumes less than 1.73π , beyond which solutions do not exist. These unduloid shapes match quite well with those computed by Everett & Haynes (1972) using the full expression for the mean curvature; importantly, the dependence of Λ_U on the initial thickness of the film ($1 - d_0$) is well-approximated (see the [supplementary material](#)). This is not

the case if one uses the linearized expression for the curvature (obtained in the limit $1 - d_0 \ll 1$), as is done in traditional lubrication models of thin films: the resulting equation is linear in g and yields unduloids with a fixed, d_0 -independent, width of 2π (Lister *et al.* 2006). So, in addition to pinchoff dynamics (Dietze & Ruyer-Quil 2015), the shape of unduloids is another qualitative feature that necessitates the use of the $\mathcal{O}(\epsilon^2)$ WRIBL model.

The variation of D_f predicted by (4.2) is plotted as a solid-black line in figure 8(a) and seen to agree rather well with the simulations. Importantly, the increase in D_f with the mucus volume can now be understood in terms of the change in the unduloid's shape, which is illustrated in figures 8(b-d). Here, we also overlay the final profile of the film (red-dashed line) from the simulations, on top of the unduloid (gray shading); despite the use of a precursor film, the simulated interface profile agrees rather well with the conceptual ideal of an equilibrium unduloid and a fully-depleted zone. Now, as the film thickness increases, destabilizing capillary forces due to the radial curvature increase in strength relative to stabilizing axial-curvature forces. As a result, the unduloids (and the corresponding humps in the simulations) become deeper, so much so that their length Λ_U reduces even as the total volume increases. The wavelength of the fastest-mode Λ_{RP} also decreases, but not as much as Λ_U . The net effect therefore is that a larger portion of the wall is left devoid of mucus.

The small variation in D_f among the different random simulations (see the small error bars in figure 8(a)) confirms our expectation that regardless of the details of the initial perturbation (so long as it triggers the fastest-growing mode of the Rayleigh-Plateau instability) the film ultimately evolves into an unduloid-shaped hump with an adjacent depleted zone. A complete understanding of the role of random perturbations, though, requires an analysis of simulations on long domains that span multiple wavelengths of the fastest growing mode. Our ongoing work in this direction shows that (4.2) remains a good approximation to D_f even on long domains. We comment further on this point in our concluding remarks in § 6.

An important consequence of (4.2) is that the minimum value of D_f , attained in the limit of a vanishingly-thin film ($d_0 \rightarrow 1$), is far from zero—approximately 0.30 as seen from the solid line in figure 8(a). (This limiting value is what is predicted when using the linearized expression for the curvature, as shown in the [supplementary material](#).) So, an appreciable fraction of the wall is always depleted of mucus, leaving it vulnerable to airborne particles. And adding more mucus only worsens the situation by producing deeper but shorter humps that expose even more of the wall. Does this increased exposure imply that more particles will deposit on the wall when more mucus is present, or will the deeper humps be able to trap more particles? We directly address this question, for particles spanning a wide range of sizes, in the next section.

5. Particle transport and deposition

We consider two different scenarios in this study of particle deposition, which correspond to two extremes of inter-breath particle-turnover. In the first scenario, the same particles persist within the airway throughout the simulation, which spans 30 breathing cycles (30 seconds). In the second scenario, we assume that all particles are replaced by fresh ones after each breath, due to mixing between tidal air and reserve air or between neighbouring airways (Altshuler *et al.* 1959; Wang 2005, chap 5).

A number concentration of $300 \mu\text{g m}^{-3}$, which is typical for $\text{PM}_{2.5}$ (epa.gov 2024), translates to about 16 micron-sized particles in the airway under consideration. So, in the first scenario, we introduce 16 particles into the periodic airway-domain, at random locations, and track their motion for 30 seconds (while removing particles that deposit on the film). We then perform an ensemble of 125 such simulations, each starting from a different random initial-distribution of particles. We thus obtain good statistics for deposition results, such as $\phi(t)$, the fraction of particles that have deposited (on the wall or mucus) at any time during the simulation. Now,

because the particles do not interact with each other in the simulation, the mean value of ϕ obtained from the ensemble of 125 simulations would be identical to the value obtained from a single simulation with $16 * 125 = 2000$ particles. Hence, the chosen number concentration, *i.e.*, the number of particles introduced into the airway in each simulation, will only affect the variance in the deposition fraction and not the ensemble-averaged mean results.

In the second scenario, we again introduce 16 particles at random locations in the airway and track them for one breathing cycle; we then remove all non-trapped particles and introduce a fresh set of 16 particles. This process is repeated for 30 breathing cycles (30 second of respiration). We then perform an ensemble of 60 such simulations. Of course, because the particles are replaced after each cycle, this calculation is equivalent to running an ensemble of 1800 simulations, each for one breathing cycle.

From the perspective of particle transport, the key difference between the two scenarios is that only in the first scenario will the distribution of particles have sufficient time to respond to the non-homogeneous nature of the flow field. For example, the curved streamlines of the airflow near the mucus hump will induce a slight centrifugal-drift of weakly inertial particles towards the centreline, which in the first scenario will add up from breath to breath to produce an accumulation of particles near the centreline. Such accumulative effects will not occur in the second scenario, wherein complete turnover of particles takes place after each breath.

While discussing our results we shall distinguish between deposition on the mucus humps (mucus entrapment) and deposition on the mucus-depleted zones (wall deposition). In the latter case, the particles deposit not directly on the epithelial cells of the airway wall, but rather on the PCL layer which our model ignores. Nevertheless, we shall, for simplicity, use the term wall-deposition because these particles are much more likely to reach the wall through the thin, low-viscosity, PCL layer than through the combination of the thick, viscous, mucus hump followed by the PCL layer.

In § 3.2, we had noted that the air flow was orders of magnitude faster than the cilia-induced translation of the interface and so we had anticipated that ciliary transport will not affect particle deposition. We have checked this and indeed found that our deposition results remain unaffected by decreasing $\langle u_c \rangle$ by a factor of ten. So, though ciliary transport is present in the particle-transport simulations, it does not contribute to deposition.

Let us begin with the first scenario and examine how the deposition fraction ϕ depends on the particle size. Results obtained after 30 breathing cycles (30 seconds) are presented in figure 9(a) for a relatively thick film. Three curves of ϕ are shown, corresponding to the fraction of particles deposited on the mucus hump, on the airway wall (depleted zone), and on either surface (total deposition). The particle size is represented by Pe and St (see (2.38) and table 3); recall that Pe represents the importance of convection relative to Brownian-diffusion, while St indicates the importance of particle inertia. Both Pe and St increase with size, so that the particle motion changes from diffusive to tracer-like to inertial. This varying nature of particle motion may be appreciated by comparing supplementary [movie 1](#) with [movie 2](#) and [movie 3](#), which illustrate the motion of particles with $Pe = 2 \times 10^4$ ($St = 9 \times 10^{-7}$), $Pe = 9 \times 10^5$ ($St = 2 \times 10^{-3}$), and $Pe = 9 \times 10^6$ ($St = 2 \times 10^{-1}$), respectively. (These movies use a large number of particles to better visualize the qualitative features of their motion.)

Figure 9(a) shows that the total deposition initially decreases with particle size, as the strength of Brownian forces reduce. However, there is an increase of deposition for the larger, inertial particles. That this significant increase is associated with the presence of a deep mucus hump is demonstrated by comparing figure 9(a) with figure 9(b). In the latter, which corresponds to a much thinner film with a shallow hump, the deposition fraction remains very small even for inertial particles.

The non-monotonic variation of total deposition with particle size, seen in figure 9(a), is a well known feature of experimental measurements of deposition in the lungs (Morawska *et al.* 2022).

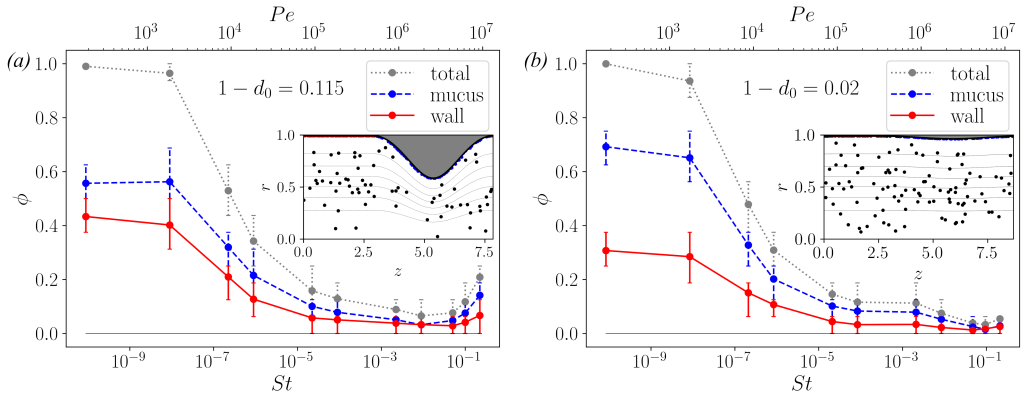


FIG. 9. Deposition fraction ϕ as a function of particle size, after 30 breathing cycles (scenario one), in an airway with (a) a relatively thick film, $1 - d_0 = 0.115$, and (b) a very thin film, $1 - d_0 = 0.02$. The particle size is represented by the corresponding values of St (bottom axis) and Pe (top axis). Snapshots of the two films, in their long-term asymptotic states, are shown as insets in the corresponding panels. For each particle size, the marker represents the mean of the distribution of ϕ , obtained from the ensemble of 125 simulations; the bar corresponds to the interquartile range which is indicative of the spread of the distribution. The fraction of particles depositing on the mucus hump, the depleted-zone of the wall, and on either surface are shown separately (see the legend).

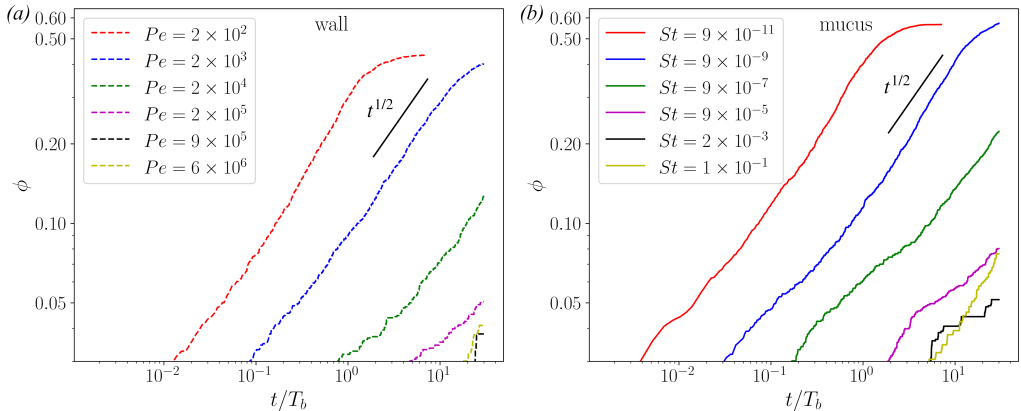


FIG. 10. Evolution of the ensemble-averaged deposition fraction on (a) the depleted-zones of the wall and (b) the mucus hump. Results are shown for six different particles sizes; for convenience, both the Pe and St values of these particles are mentioned in the legend, which is split across the two panels. The solid-black line corresponds to a growth of $t^{1/2}$.

However, the increase for inertial particles is much stronger in entire-lung measurements because the effects of particle inertia are very strong in the turbulent flows of the upper airways, as well as in the secondary circulatory flows at airway bifurcations (Guha 2008). Here, we see that a non-monotonic variation of deposition, albeit weaker, arises even in a single airway provided the mucus film is thick enough to form prominent humps.

The variation of the deposition fraction with time, for different particle-sizes, is presented in figure 10. The small particles, whose deposition is driven by Brownian motion, naturally exhibit an approximate $t^{1/2}$ diffusive growth of ϕ . Given sufficient time, all these particles will be deposited on either the wall or the mucus humps. The effects of inertia are first seen for $St = 2 \times 10^{-3}$, for which ϕ saturates to a low value (figure 10b). As shown below, the cessation of further deposition is a result of gradual centrifugal migration towards the centreline, owing to

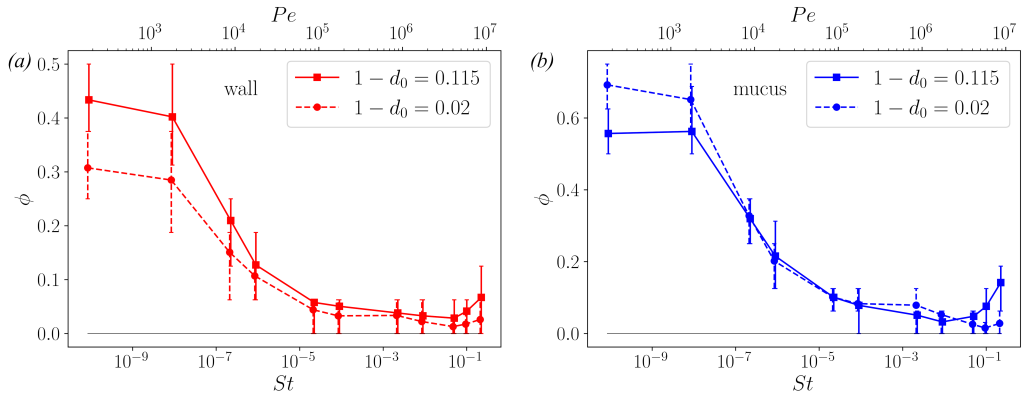


FIG. 11. Effect of the initial film thickness (mucus volume) on the deposition fraction. The results from figures 9(a-b) are overlapped for deposition on (a) the depleted-zone of the wall, and (b) the mucus hump.

the curved air streamlines below the mucus hump. As these inertial forces become stronger, the particles veer-off from streamlines more violently and collide with the mucus hump; hence the increase in deposition for the largest particle with $St = 2 \times 10^{-1}$ (figure 10b).

Returning to figure 9(a), let us examine the difference between the deposition on the mucus hump (blue dashed line) and on the exposed wall (red solid line). For the small particles, we see that though a higher fraction deposit on the mucus hump, a significant fraction does reach the wall. The difference between the deposition fractions mirrors the difference in the surface areas of the mucus hump and the exposed wall (55% and 45%, respectively, of the total surface area exposed to air). This correspondence is a sign of the diffusive nature of deposition of the small particles (see in particular the values for the smallest particle with $Pe = 2 \times 10^2$). The deposition of inertial particles on the hump and the wall is governed by other physical effects and will be discussed later in this section.

Next, let us examine the effect of the mucus volume fraction with the aid of figure 11, which overlaps the results for the two film thickness shown previously in figures 9(a-b). We have already seen that thicker films produce larger mucus-depleted zones (see figure 8a). One would expect the widening of depleted zones to allow more small Brownian particles to deposit on the wall when the film is thicker. This is exactly what we observe in figure 11(a). Consequently, a smaller fraction of small particles is entrapped by the mucus humps in the case of the thicker film (figure 11b). These differences between the two films are less for the larger tracer-like particles, which diffuse more slowly. However, deposition of the largest, inertial particles is again markedly higher for the thicker film—especially on the mucus hump—owing to inertial effects.

Inertia causes the large particles to deviate from the air streamlines and collide with the wall and the mucus hump. When heavy particles approach the mucus hump, their inertia prevents them from going around the hump along with the curved streamlines. Instead, they continue moving straight and collide with the mucus hump. Evidence for such inertial impactation (Guha 2008) is provided by the collision velocity, $V_{||}$, which is the relative velocity between the particle and the deposition site (mucus hump or wall) at the time of deposition, projected along the approach direction. Figure 12 presents the mean collision velocity of particles with the mucus hump (panel a) and the wall (panel b) for the case of the thick film (figure 9a); here, the bars represent the interquartile range which is indicative of the spread of the distribution of $V_{||}$. The smallest diffusive particles have a large $V_{||}$ because of the dominance of fluctuating Brownian forces. The tracer-like particles have a very low $V_{||}$, as expected for particles whose velocity is almost entirely aligned with the air streamlines which are tangential to the mucus hump and the wall. The relatively large, inertial particles though show a marked increase in $V_{||}$, especially for collisions with the mucus

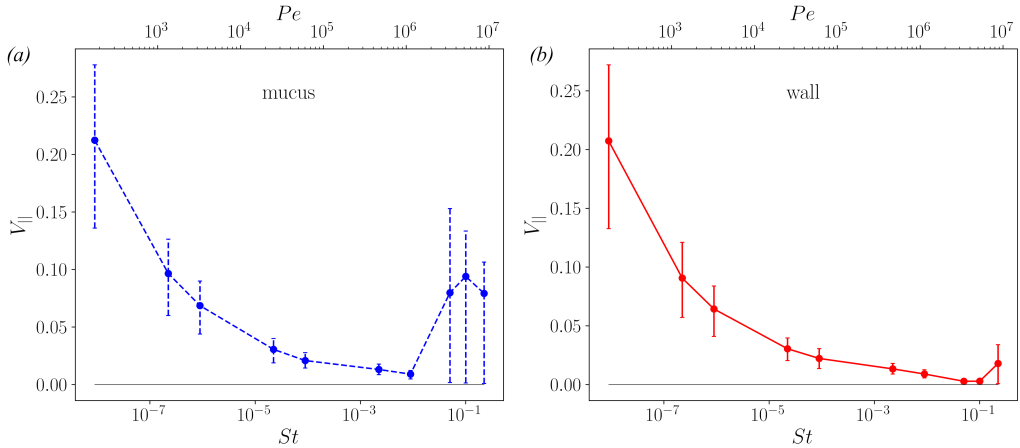


FIG. 12. Collision velocity $V_{||}$ of particles with the depositing surface: (a) mucus hump, (b) depleted-zone of the wall. The marker and the bar represents the mean and the inter-quartile-range (which measures the variation about the mean) of the distribution of $V_{||}$ for each particle size. These results correspond to the case of the relatively thick film in figure 9(a).

hump which protrudes into the airway (figure 12a); as anticipated, inertial particles deviate from the streamlines and collide with the mucus hump.

The slight decrease in $V_{||}$ for the collisions of the largest particle with the hump (compare the second-largest with the largest particle in figure 12a) signifies the growing influence of the particle interception effect (Guha 2008): Because of its increasing radius, the centre of the particle need not deviate as strongly from the airflow streamlines in order for the particle surface to make contact with the mucus film. Thus, deposition will include more low-velocity collisions as the particle size increases.

The collision velocity of inertial particles with the wall is much smaller than that with the hump, even for the largest particle (compare figures 12a-b). Deposition on the wall, though, is aided by the non-uniform number concentration of inertial particles in the airway: a subtle interplay of varying airflow speed and streamline-curvature leads to an elevated number concentration near the depleted zone on the wall.

The spatial distribution of particles is examined in figure 13. The mean radial location of all non-trapped particles, $\langle r \rangle_p$, is plotted as a function of time in figure 13(a). The gradual migration towards the centreline, $r = 0$, is apparent here for the relatively-large inertial particles; such migration does not occur for the small diffusive particles. The small oscillations in $\langle r \rangle_p$, present for all particles, are a result of the axisymmetric geometry and the converging-diverging nature of the air streamlines, which causes a small convergence toward the centreline, followed by a corresponding divergence, each time particles are carried past the hump. These oscillations do not lead to a net convergence, though, and the preferential concentration near the centreline is caused by gradual inertial centrifugation.

The probability distribution function (pdf) of the radial location of non-trapped particles, integrated over time, is shown in figure 13(b). The main panel reinforces the message of figure 13(a), that small particles are uniformly distributed, while inertial particles accumulate near the centreline. The inset, though, reveals a surprising accumulation of inertial particles near the depleted zone of the wall (there is no accumulation below the hump which extends up to $r \approx 0.6$). Supplementary movie 3 shows how heavy particles that begin near the depleted zone tend to remain there (though the majority of particles, which at some time pass by the hump, are centrifuged towards the centreline). This is due, in part, to the low air-velocity near the depleted

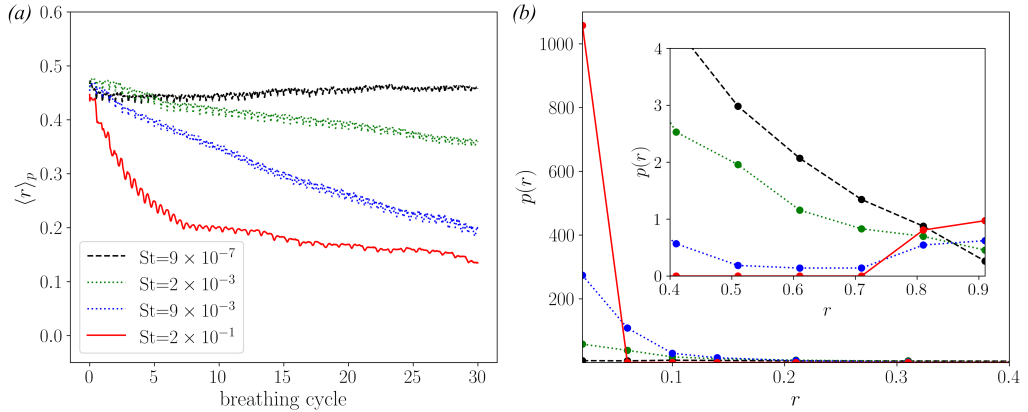


FIG. 13. Non-homogeneous distribution of particles in the airway, for the case of the relatively thick film (see figure 9a). (a) Evolution of the mean radial location of particles (non-deposited) in the airway; the migration of inertial particles ($St = 0.009, 0.2$) towards the centreline is clearly visible. (b) The probability distribution function of the radial location of particles, integrated over time (data from $t = 0$ to $t = 30T_b$ is used to construct the distribution). The distribution near the centreline is shown in the main panel, while that near the wall is shown in the inset.

zone (which has the highest cross-sectional flow area). Over a breathing cycle, the particles travel only a short way past the edge of the hump before returning to the depletion zone, and hence they do not pass the bottom of the hump where the centrifugation towards the centreline acts most strongly. On the contrary, because the curvature of the streamlines near the edge of the depletion zone (where it meets the hump) is opposite to that of the streamlines below the hump, the inertial particles are weakly pushed towards the edge of the depletion zone.

To summarize the results of the first scenario, there is a non-monotonic variation of deposition with particle size because small particles deposit due to Brownian forces and large particles deposit due to inertial effects. The latter are rather subtle: strong centrifugal forces near mucus humps produce high-velocity collisions, whereas weak centrifugal forces near mucus-depleted zones of the wall cause particles to accumulate and then gradually deposit there.

Let us now turn to the second scenario. The deposition fraction here will be smaller than in the first scenario because the particles have just one breathing cycle (instead of thirty) in which to deposit before they are replaced by new particles. At the same time, the airway in the second scenario is exposed to far more particles, in total. So, while interpreting the magnitude of ϕ , one should bear in mind that the number of deposited particles in the first and second scenarios is given by 16ϕ and $(16 \times 30)\phi$, respectively. In the following discussion of the second scenario, we shall examine how ϕ changes with the particle size, in light of the corresponding variation in the first scenario.

Because the particles are replaced very frequently, the inertial particles will not have time to accumulate near the centreline or near the wall, as they did in scenario one (figure 13b). Therefore, while particle inertia should still promote deposition on the mucus hump due to centrifugation and high-velocity collisions, there should not be any wall-deposition due to inertia because particles will not accumulate near the wall in scenario two. This is exactly what we see in figure 14, which compares the results for deposition on the mucus hump (panel a) and on the mucus-depleted portion of the wall (panel b), for the two cases of a thick and a thin film (see the legend). More inertial particles are trapped by the thicker film with the deeper mucus hump (see the inset of figure 14a and note the significant relative increase of ϕ for the largest particle). As anticipated, there is no such increase in the case of wall-deposition of inertial particles (see the inset of figure 14b). For small diffusive particles, we see that, just as in scenario one, the thicker mucus

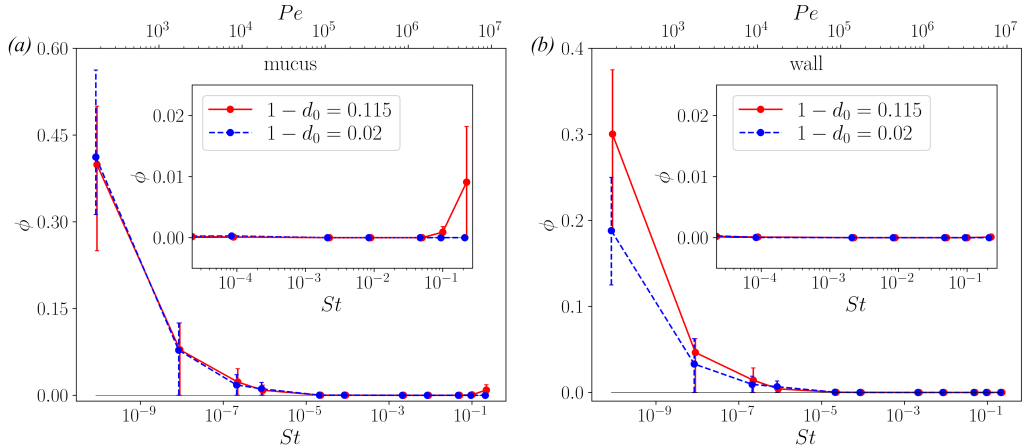


FIG. 14. Variation of the deposition fraction ϕ with particle size, for the second scenario in which particles are replaced after each breath. Results for the thick and thin film are compared for deposition on (a) the mucus hump and (b) the wall. The insets are zooms that show the variation of ϕ for the large particles. The markers and the bars represent the mean and the inter-quartile-range of the deposition fraction measured from an ensemble of 60 simulations, each run for 30 breathing cycles (a total of 1800 breaths between which particles are entirely replaced).

film allows more particles to deposit on the wall because of the presence of larger mucus-depleted zones (figure 14b).

The key takeaway from the results of the second scenario is that particle turnover counter-acts the effects of inertia-driven preferential accumulation. So, if a substantial fraction of particles in an airway are replaced after each breath (thanks to mixing between airways or between tidal and reserve air volumes), then a higher mucus volume will not cause more wall-deposition of heavy inertial particles. Taken together, the two scenarios suggest that the primary effects of increasing the mucus volume fraction are more mucus-entrapment of large inertial particles and more wall-deposition of small diffusive particles. Which of these opposing outcomes is detrimental or beneficial to human health depends on the nature of the particles—harmful allergens and pathogens, or therapeutic drugs.

6. Concluding remarks

We have studied the transport of aerosols in a ciliated mucus-bearing airway with the aim of understanding how the distribution of the mucus film, and the airflow around it, affects particle deposition. Considering a typical mid-generation airway, our simulations and analyses have shown that the mucus distribution is unaffected by airflow, which is too weak (under normal breathing conditions) to compete with the capillary forces that determine the final shape of the mucus interface. Ciliary transport also does not alter the interface profile but simply translates it. The speed of translation is orders-of-magnitude slower than the velocity of airborne particles and so ciliary transport has no impact on the nature or rate of deposition.

While a thick film will pinch-off (and form a liquid bridge that occludes the airway), a sufficiently thin film will remain open, organizing itself into unduloid-shaped annular humps separated by depleted zones. Focusing on open airways, we have investigated the transport of air-borne particles spanning a wide range of sizes. We have seen that the distribution of mucus into humps and depleted zones significantly impacts particle deposition, and in a manner than depends on the particle size. Our counterintuitive finding, that thicker mucus films produce larger depleted zones, results in more small (diffusive) particles depositing on the wall, as the amount of

mucus is increased. For large (inertial) particles, however, a thicker film aids in mucus entrapment by producing deeper humps that intercept more particles.

The analysis in this work has been based entirely on a periodic domain of length equal to the wavelength of the fastest-growing Rayleigh-Plateau mode. Typical mid-generation airways have lengths that are up to two to four times longer (table 1). So, our results will apply to long airways if the film organizes itself into a repeating pattern with wavelength roughly equal to that of the fastest mode. This dominance of the fastest-growing instability mode, first hypothesized by Rayleigh (1879), is typically true in problems of interfacial pattern formation like Rayleigh-Plateau and Rayleigh-Taylor, with the exception of special circumstances in which the linear-growth-rate curve (dispersion relation) exhibits multiple peaks (Picardo & Narayanan 2017). For the present problem, we expect Rayleigh's paradigm to hold. We are currently testing this expectation by comparing the results of long domain simulations, spanning multiple fastest-mode wavelengths, against those of the short, single-wavelength domain. With regard to the extent of mucus-depleted zones, our results (to be reported elsewhere) show that the analysis of § 4 works reasonably well even on long domains.

Several interesting, physiologically-relevant extensions to our study are possible. For example, one could incorporate allergen-induced mucus secretion (Gauvreau *et al.* 2015), such that the deposition of particles on the wall triggers a release of mucus (Spungin & Silberberg 1984). Such a model would shed light on the rapid blockage of airways by mucus plugs (liquid bridges), as occurs in cases of sudden-onset fatal asthma (Hays & Fahy 2003; Rogers 2004). The model can also be extended to describe the dynamics of the plugs so formed, by following the recent work of Dietze (2024), which represents a major advance in thin-film modelling. By detailed comparisons with volume-of-fluid based direct-numerical-simulations, Dietze (2024) shows that plugs can be faithfully described by an extended form of the WRIBL model, which was first proposed by Dietze *et al.* (2020). This model adds a source term which applies a disjoining-pressure at the centreline to stabilize the closing interface in the form of a pseudo-plug.

Our study has shown that depositing particles can avoid mucus due to the ever-present mucus-depleted zones along the wall. While such direct deposition of particles certainly poses a threat to the health of the airway, even the particles that are intercepted by mucus humps could still find their way, through the mucus, to the wall. While studying in-mucus transport, it will be important to consider the non-Newtonian rheology of mucus, which affects particle transport by altering not only the diffusive motion of particles (Hill *et al.* 2014) but also the active motility of microorganisms like bacteria (Lauga 2020; Pednekar *et al.* 2022).

Acknowledgements. J.R.P. acknowledges his Associateship with the International Centre for Theoretical Sciences (ICTS), Tata Institute of Fundamental Research, Bangalore, India. In particular, he is very grateful for the warm hospitality he received at ICTS during the writing of this paper. The authors thank the National PARAM Supercomputing Facility *PARAM SIDDHI-AI* at CDAC, Pune for computing resources; simulations were also performed on the IIT Bombay workstations *Gandalf* (procured through DST-SERB grant SRG/2021/001185), and *Faramir* and *Aragorn* (procured through the IIT-B grant RD/0519-IRCCSH0-021).

Funding. This work was supported by DST-SERB (J.R.P., grant no. SRG/2021/001185), the Indo-French Centre for the Promotion of Advanced Scientific Research (IFCPAR / CEFIPRA) (J.R.P. project no. 6704-A), and IRCC, IIT Bombay (S.H., Ph.D. fellowship; J.R.P., grant no. RD/0519-IRCCSH0-021).

Author ORCID. S. Hazra, <https://orcid.org/0009-0000-3728-5888>; J. R. Picardo, <https://orcid.org/0000-0002-9227-5516>

Appendix A. Validation with Dietze & Ruyer-Quil (2015)

As a check on our derivation of the WRIBL equations, and to validate our numerical simulations, we have compared our results with those reported in Dietze & Ruyer-Quil (2015) and found excellent agreement. An example is shown in figure 15, which plots the time trace of the maximum and minimum of the interface

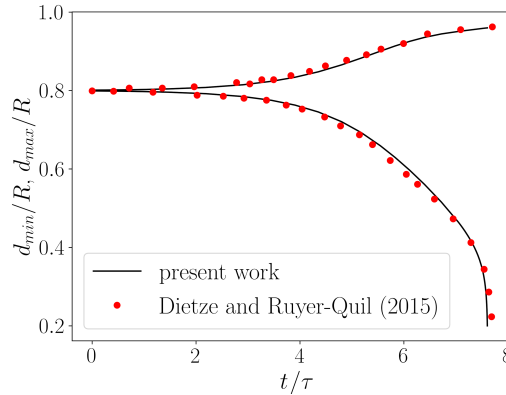


FIG. 15. Comparison of a simulation of the fully-coupled WRIBL model with the corresponding results from figure 3(d) of Dietze & Ruyter-Quil (2015). The latter data (red markers) were approximated using the data extraction tool in Origin (OriginLab, USA). The evolution of the minimum and maximum radial position of the interface is compared, for a case in which the interface pinches-off. A Jupyter notebook that simulates the WRIBL model and generates this figure is available at https://cocalc.com/share/public_paths/dade5dbc44da89bf9c905d19b83941294ff7914b.

profile for an air-mucus flow in which the interface ultimately pinches-off. Here, time is normalized by the inertialess approximation of the linear-growth timescale of the fastest-growing instability mode, which when scaled by R/U is $\tau = 6(\mu_m U d_0 / \gamma) \left(\alpha^4 (1/\alpha^2 - 1)(1/d_0 - 1)^2 (1/d_0^2 - 1) \right)^{-1}$ where $\alpha = 2\pi d_0 R / \Lambda_{RP}$.

The *Jupyter Notebook* associated with figure 15 (see the caption) demonstrates how the WRIBL equations are simulated, by first importing symbolic expressions for the coefficients from text files, then discretizing using central differences, and finally time-stepping with the LSODA algorithm using the `solve_ivp` function in Python.

References

- Aghaei, Y., Sajadi, B. & Ahmadi, G. 2023 The effect of the mucus layer and the inhaled air conditions on the droplets fate in the human nasal cavity: A numerical study. *J. Aerosol Sci.* **171**, 106163.
- Altshuler, B., Palmes, E. D., Yarmus, L. & Nelson, N. 1959 Intrapulmonary mixing of gases studied with aerosols. *J. Appl. Physiol.* **14** (3), 321–327.
- Bagheri, F., Mitra, D., Perlekar, P. & Brandt, L. 2012 Statistics of polymer extensions in turbulent channel flow. *Phys. Rev. E* **86**, 056314.
- Beelen, R., Raaschou-Nielsen, O., Stafoggia, M., Andersen, Z. J., Weinmayr, G., Hoffmann, B., Wolf, K., Samoli, E. and Fischer, P., Nieuwenhuijsen, M. & others 2014 Effects of long-term exposure to air pollution on natural-cause mortality: an analysis of 22 european cohorts within the multicentre escape project. *Lancet* **383** (9919), 785–95.
- Blake, J. 1975 On the movement of mucus in the lung. *J. Biomech.* **8** (3-4), 179–190.
- Blake, J. 2001 Fluid mechanics of ciliary propulsion. In *Computational Modeling in Biological Fluid Dynamics* (ed. L. J. Fauci & S. Gueron), pp. 1–51. Springer New York.
- Bottier, M., Blanchon, S., Pelle, G., Bequignon, E., Isabey, D., Coste, A., Escudier, E., Grotberg, J. B., Papon, J. F., Filoche, M. & others 2017a A new index for characterizing micro-bead motion in a flow induced by ciliary beating: Part i, experimental analysis. *PLOS Comput. Biol.* **13** (7), 1–19.
- Bottier, M., Peña Fernández, M., Pelle, G., Isabey, D., Louis, B., Grotberg, J. B. & Filoche, M. 2017b A new index for characterizing micro-bead motion in a flow induced by ciliary beating: Part ii, modeling. *PLOS Comput. Biol.* **13** (7), 1–21.
- Button, B., Cai, L. H., Ehre, C., Kesimer, M., Hill, D. B., Sheehan, J. K., Boucher, R. C. & Rubinstein, M. 2012 A periciliary brush promotes the lung health by separating the mucus layer from airway epithelia. *Science* **337** (6097), 937–941.
- Chakrabarti, B., Furthauer, S. & Shelley, M. J. 2022 A multiscale biophysical model gives quantized metachronal waves in a lattice of beating cilia. *PNAS* **119** (4), e2113539119.

- Chakrabarti, B. & Saintillan, D. 2019 Hydrodynamic synchronization of spontaneously beating filaments. *Phys. Rev. Lett.* **123**, 208101.
- Chatelin, R. & Poncet, P. 2016 A parametric study of mucociliary transport by numerical simulations of 3d non-homogeneous mucus. *J. Biomech.* **49** (9), 1772–1780.
- Choudhury, A., Filoche, M., Ribe, N. M., Grenier, N. & Dietze, G. F. 2023 On the role of viscoelasticity in mucociliary clearance: a hydrodynamic continuum approach. *J. Fluid Mech.* **971**, A33.
- Dietze, G. F. 2024 Liquid plugs in narrow tubes: application to airway occlusion. *J. Fluid Mech.* **998**, A50.
- Dietze, G. F., Lavalle, G. & Ruyer-Quil, C. 2020 Falling liquid films in narrow tubes: occlusion scenarios. *J. Fluid Mech.* **894**, A17.
- Dietze, G. F. & Ruyer-Quil, C. 2013 Wavy liquid films in interaction with a confined laminar gas flow. *J. Fluid Mech.* **722**, 348–393.
- Dietze, G. F. & Ruyer-Quil, C. 2015 Films in narrow tubes. *J. Fluid Mech.* **762**, 68–109.
- epa.gov 2024 Final updates to the air quality index (aqi) for particulate matter. <https://www.epa.gov/system/files/documents/2024-02/pm-naaqs-air-quality-index-fact-sheet.pdf>.
- Erken, O., Fazla, B., Muradoglu, M., Izbassarov, D., Romanò, F. & Grotberg, J. B. 2023 Effects of elastoviscoplastic properties of mucus on airway closure in healthy and pathological conditions. *Phys. Rev. Fluids* **8**, 053102.
- Erken, O., Romanò, F., Grotberg, J. B. & Muradoglu, M. 2022 Capillary instability of a two-layer annular film: an airway closure model. *J. Fluid Mech.* **934**.
- Everett, D. H. & Haynes, J. M. 1972 Model studies of capillary condensation. i. cylindrical pore model with zero contact angle. *J. Colloid Interface Sci.* **38** (1), 125–137.
- Farnoud, A., Tofighian, H., Baumann, I., Garcia, G. J. M., Schmid, O., Gutheil, E. & Rashidi, Mohammad M. 2020 Large eddy simulations of airflow and particle deposition in pulsating bi-directional nasal drug delivery. *Phys. Fluids* **32** (10), 101905.
- Fu, P., Guo, X., Cheung, F. M. H. & Yung, K. K. L. 2019 The association between pm2.5 exposure and neurological disorders: A systematic review and meta-analysis. *Sci. Total Environ.* **655**, 1240–1248.
- Fulford, G. R. & Blake, J. R. 1986 Muco-ciliary transport in the lung. *J. Theor. Biol.* **121** (4), 381–402.
- Gardiner, C. 2009 *Stochastic Methods: A Handbook for the Natural and Social Sciences*. Berlin: Springer.
- Gauvreau, G. M., El-Gammal, A. I. & O'Byrne, P. M. 2015 Allergen-induced airway responses. *Eur. Respir. J.* **46** (3), 819–831.
- Ghatak, A., Khanna, R. & Sharma, A. 1999 Dynamics and morphology of holes in dewetting of thin films. *J. Colloid Interface Sci.* **212** (2), 483–494.
- Ghorui, S., Kundu, D., Chakravarty, A. & Panchagnula, M. V. 2024 The impact of asymmetric branching on particle deposition in conducting airways. *Int. J. Multiph. Flow* **179**, 104935.
- Gilpin, W., Bull, M. S. & Prakash, M. 2020 The multiscale physics of cilia and flagella. *Nat. Rev. Phys.* **2**, 74–88.
- Grabowski, W. W. & Wang, L.-P. 2013 Growth of cloud droplets in a turbulent environment. *Annu. Rev. Fluid Mech.* **45**, 293.
- Gsell, S., Loiseau, E., D'Ortona, U., Viallat, A. & Favier, J. 2020 Hydrodynamic model of directional ciliary-beat organization in human airways. *Sci. Rep.* **10**, 8405.
- Guha, A. 2008 Transport and deposition of particles in turbulent and laminar flow. *Annu. Rev. Fluid Mech.* **40**, 311–341.
- Guo, H., Fauci, L., Shelley, M. & Kanso, E. 2018 Bistability in the synchronization of actuated microfilaments. *J. Fluid Mech.* **836**, 304–323.
- Halpern, D., Fujioka, H. & Grotberg, J. B. 2010 The effect of viscoelasticity on the stability of a pulmonary airway liquid layer. *Phys. Fluids* **22** (1), 011901.
- Hays, S. R. & Fahy, J. V. 2003 The role of mucus in fatal asthma. *Am. J. Med.* **115** (1), 68–69.
- Hegedüs, Cs.J., Balásházy, I. & Farkas, Á. 2004 Detailed mathematical description of the geometry of airway bifurcations. *Respir. Physiol. Neurobiol.* **141** (1), 99–114.
- Heil, M., Hazel, A. L. & Smith, J. A. 2008 The mechanics of airway closure. *Respir. Physiol. Neurobiol.* **163** (1-3), 214–221.
- Heyder, J., Gebhart, J., Rudolf, G., Schiller, C. F. & Stahlhofen, W. 1986 Deposition of particles in the human respiratory tract in the size range 0.005–15 μm . *J. Aerosol Sci.* **17** (5), 811–825.
- Hill, D. B., Vasquez, P. A., Mellnik, J., McKinley, S. A., Vose, A., Mu, F., Henderson, A. G., Donaldson, S. H., Alexis, N. E., Boucher, R. C. & others 2014 A biophysical basis for mucus solids concentration as a candidate biomarker for airways disease. *PloS one* **9** (2), e87681.

- Hindmarsh, A. C. & Petzold, L. R. 1995 Algorithms and software for ordinary differential equations and differential-algebraic equations, part ii: Higher-order methods and software packages. *Comput. Phys.* **9** (2), 148–155.
- Ireland, P. J., Vaithianathan, T., Sukheswalla, P. S., Ray, B. & Collins, L. R. 2013 Highly parallel particle-laden flow solver for turbulence research. *Comput. Fluids* **76**, 170–177.
- Johns, L. E. & Narayanan, R. 2002 *Interfacial Instability*. Springer.
- Kalliadasis, S., Ruyer-Quil, C., Scheid, B. & Velarde, M. G. 2012 *Falling Liquid Films*. Springer.
- Keeler, J. A., Patki, A., Woodard, C. R. & Frank-Ito, D. O. 2016 A computational study of nasal spray deposition pattern in four ethnic groups. *J. Aerosol Med. Pulm. Drug Deliv.* **29** (2), 153–166.
- Kim, C. S., Abraham, W. M., Chapman, G. A. & Sackner, M. A. 1985 Influence of two-phase gas-liquid interaction on aerosol deposition in airways. *Am. Rev. Respir. Dis.* **131** (4), 618–623.
- Kim, C. S. & Eldridge, M. A. 1985 Aerosol deposition in the airway model with excessive mucus secretions. *J. Appl. Physiol.* **59** (6), 1766–1772.
- Kleinstreuer, C. & Zhang, Z. 2010 Airflow and particle transport in the human respiratory system. *Annu. Rev. Fluid Mech.* **42**, 301–334.
- Knowles, M. R. & Boucher, R. C. 2002 Mucus clearance as a primary innate defense mechanism for mammalian airways. *J. Clin. Invest.* **109** (5), 571–577.
- Kumar, P., Jutur, P., Roy, A. & Panchagnula, M. 2024 Evidence of chaotic mixing in the alveolar region of the lung. arXiv:2403.13917.
- Lansley, A. B. 1993 Mucociliary clearance and drug delivery via the respiratory tract. *Adv. Drug Deliv. Rev.* **11** (3), 299–327, relevance of Mucus to Advanced Drug Delivery.
- Lauga, E. 2020 *Locomotion and Transport in Complex Fluids*, p. 315–352. Cambridge University Press.
- Levy, R., Hill, D. B., Forest, M. G. & Grotberg, J. B. 2014 Pulmonary fluid flow challenges for experimental and mathematical modeling. *Integr. Comp. Biol.* **54**, 985–1000.
- Li, A. & Ahmadi, G. 1995 Computer simulation of particle deposition in the upper tracheobronchial tree. *Aerosol Sci. Tech.* **23** (2), 201–223.
- Lin, C. L., Tawhai, M. H., McLennan, G. & Hoffman, E. A. 2007 Characteristics of the turbulent laryngeal jet and its effect on airflow in the human intra-thoracic airways. *Respir. Physiol. Neurobiol.* **157** (2), 295–309.
- Lister, J. R., Rallison, J. M., King, A. A., Cummings, L. J. & Jensen, O. E. 2006 Capillary drainage of an annular film: the dynamics of collars and lobes. *J. Fluid Mech.* **552**, 311–343.
- Liu, C., Xue, C., Sun, J. & Hu, G. 2016 A generalized formula for inertial lift on a sphere in microchannels. *Lab Chip* **16**, 884–892.
- Maxey, M. R. 1987 The gravitational settling of aerosol particles in homogeneous turbulence and random flow fields. *J. Fluid Mech.* **174**, 441–465.
- Maxey, M. R. & Riley, J. J. 1983 Equation of motion for a small rigid sphere in a nonuniform flow. *Phys. Fluids* **26** (4), 883–889.
- Meurer, A., Smith, C. P., Paprocki, M., Čertík, O., Kirpichev, S. B., Rocklin, M., Kumar, A., Ivanov, S., Moore, J. K., Singh, S. & others 2017 Sympy: symbolic computing in python. *PeerJ Comput. Sci.* **3**, e103.
- Mitran, S. M. 2007 Metachronal wave formation in a model of pulmonary cilia. *Comput Struct.* **85** (11-14), 763–774.
- Mittal, R., Ni, R. & Seo, J. H. 2020 The flow physics of covid-19. *J. Fluid Mech.* **894**.
- Morawska, L., Buonanno, G., Mikszewski, A. & Stabile, L. 2022 The physics of respiratory particle generation, fate in the air, and inhalation. *Nat. Rev. Phys.* **4** (11), 723–734.
- Oldenburg, A. L., Chhetri, R. K., Hill, D. B. & Button, B. 2012 Monitoring airway mucus flow and ciliary activity with optical coherence tomography. *Biomed. Opt. Express* **3** (9), 1978–1992.
- Oron, A., Davis, S. H. & Bankoff, S. G. 1997 Long-scale evolution of thin liquid films. *Rev. Mod. Phys.* **69** (3), 931.
- Öttinger, H. C. 1996 *Stochastic Processes in Polymeric Fluids*. Berlin: Springer.
- Pedley, T. J. 1977 Pulmonary fluid dynamics. *Annu. Rev. Fluid Mech.* **9** (1), 229–274.
- Pednekar, D. D., Liguori, M. A., Marques, C. N. H., Zhang, T., Zhang, N., Zhou, Z., Amoako, K. & Gu, H. 2022 From static to dynamic: A review on the role of mucus heterogeneity in particle and microbial transport. *ACS Biomater. Sci. Eng.* **8** (7), 2825–2848.
- Picardo, J. R. & Narayanan, R. 2017 Interfacial pattern selection in defiance of linear growth. *J. Fluid Mech.* **829**, 345–363.

- Quek, Y. L. R., Lim, K. M. & Chiam, K. H. 2018 Three-dimensional computational model of multiphase flow driven by a bed of active cilia. *Comput. Fluids* **170**, 222–235.
- Rahimi-Gorji, M., Pourmehran, O., Gorji-Bandpy, M. & Gorji, T. B. 2015 Cfd simulation of airflow behavior and particle transport and deposition in different breathing conditions through the realistic model of human airways. *J. Mol. Liq.* **209**, 121–133.
- Randell, S. H. & Boucher, R. C. 2006 Effective mucus clearance is essential for respiratory health. *Am. J. Respir. Cell Mol. Biol.* **35** (1), 20–28.
- Ravichandran, S., Deepu, P. & Govindarajan, R. 2017 Clustering of heavy particles in vortical flows: a selective review. *Sādhanā* **42** (4), 597–605.
- Ravichandran, S., Picardo, J. R., Ray, S. S. & Govindarajan, R. 2020 *Fluid Dynamics in Clouds*, pp. 1–23. Springer Berlin Heidelberg.
- Rayleigh, L. 1879 On the instability of liquid jets. *Proc. Lond. Math. Soc.* **10**, 4–13.
- Rayleigh, L. 1892 On the instability of cylindrical fluid surfaces. *Phil. Mag.* **34** (207), 177–180.
- Rogers, D. F. 2004 Airway mucus hypersecretion in asthma: an undervalued pathology? *Curr. Opin. Pharmacol.* **4** (3), 241–250.
- Romanò, F., Fujioka, H., Muradoglu, M. & Grotberg, J. B. 2019 Liquid plug formation in an airway closure model. *Phys. Rev. Fluids* **4**, 093103.
- Romanò, F., Muradoglu, M., Fujioka, H. & Grotberg, J. B. 2021 The effect of viscoelasticity in an airway closure model. *J. Fluid Mech.* **913**, A31.
- Romanò, F., Muradoglu, M. & Grotberg, J. B. 2022 Effect of surfactant in an airway closure model. *Phys. Rev. Fluids* **7** (9), 093103.
- Ruyer-Quil, C., Bresch, D., Gisclon, M., Richard, G. L., Kessar, M. & Cellier, N. 2023 Sliding and merging of strongly sheared droplets. *J. Fluid Mech.* **972**, A40.
- Sedaghat, M. H., Shahmardan, M. M., Norouzi, M., Jayathilake, P. G. & Nazari, M. 2016 Numerical simulation of muco-ciliary clearance: immersed boundary-lattice boltzmann method. *Comput. Fluids* **131**, 91–101.
- Singh, R. K., Picardo, J. R. & Ray, S. S. 2022 Sedimenting elastic filaments in turbulent flows. *Phys. Rev. Fluids* **7**, 084502.
- Sleigh, M. A., Blake, J. R. & Liron, N. 1988 The propulsion of mucus by cilia. *Am Rev. Respir. Dis.* **137** (3), 726–741.
- Smith, D.J. 2018 Biological fluid mechanics under the microscope: a tribute to john blake. *ANZIAM J.* **59** (4), 416–442.
- Smith, D. J., Gaffney, E. A. & Blake, J. R. 2007a Discrete cilia modelling with singularity distributions: Application to the embryonic node and the airway surface liquid. *Bull. Math. Biol.* **69**, 1477–1510.
- Smith, D. J., Gaffney, E. A. & Blake, J. R. 2007b A model of tracer transport in airway surface liquid. *Bull. Math. Biol.* **69** (3), 817–836.
- Smith, D. J., Gaffney, E. A. & Blake, J. R. 2007c A viscoelastic traction layer model of muco-ciliary transport. *Bull. Math. Biol.* **69** (1), 289–327.
- Smith, D. J., Gaffney, E. A. & Blake, J. R. 2008 Modelling mucociliary clearance. *Respir. Physiol. Neurobiol.* **163** (1-3), 178–188.
- Smith, D. J., Gaffney, E. A. & Blake, J. R. 2009 Mathematical modelling of cilia-driven transport of biological fluids. *Proc. R. Soc. Lond. A.* **465** (2108), 2417–2439.
- Spungin, B. & Silberberg, A. 1984 Stimulation of mucus secretion, ciliary activity, and transport in frog palate epithelium. *Am. J. Physiol. Cell Physiol.* **247** (5), C299–C308.
- Tsuda, A., Filipovic, N., Habertür, D., Dickie, R., Matsui, Y., Stampanoni, M. & Schittny, J. C. 2008 Finite element 3d reconstruction of the pulmonary acinus imaged by synchrotron x-ray tomography. *J. Appl. Physiol.* **105** (3), 964–976.
- Tsuda, A., Henry, F. S. & Butler, J. P. 2013 Particle transport and deposition: basic physics of particle kinetics. *Compr. Physiol.* **3** (4), 1437.
- Tsuda, A., Laine-Pearson, F. E. & Hydon, P. E. 2011 Why chaotic mixing of particles is inevitable in the deep lung. *J. Theor. Biol.* **286**, 57–66.
- Tsuda, A., Rogers, R. A., Hydon, P. E. & Butler, J. P. 2002 Chaotic mixing deep in the lung. *PNAS* **99** (15), 10173–10178.
- Vanaki, S. M., Holmes, D., Saha, S. C., Chen, J., Brown, R. J. & Jayathilake, P. G. 2020 Muco-ciliary clearance: A review of modelling techniques. *J. Biomech.* **99**, 109578.
- Vasquez, P. A., Jin, Y., Palmer, E., Hill, D. & Forest, M. G. 2016 Modeling and simulation of mucus flow in

- human bronchial epithelial cell cultures–part i: Idealized axisymmetric swirling flow. *PLoS Comput. Biol.* **12** (8), e1004872.
- Virtanen, P., Gommers, R., Oliphant, T. E., Haberland, M., Reddy, T., Cournapeau, D., Burovski, E., Peterson, P., Weckesser, W., Bright, J., others & SciPy 1.0 Contributors 2020 SciPy 1.0: Fundamental Algorithms for Scientific Computing in Python. *Nat. Methods* **17**, 261–272.
- Wang, C-S. 2005 *Inhaled Aerosols*. Elsevier.
- Wang, S. M., Inthavong, K., Wen, J., Tu, J. Y. & Xue, C. L. 2009 Comparison of micron- and nanoparticle deposition patterns in a realistic human nasal cavity. *Respir. Physiol. Neurobiol.* **166** (3), 142–151.
- Weibel, E. R., Cournand, A. F. & Richards, D. W. 1963 *Morphometry of the human lung*, , vol. 1. Springer.
- Weichenthal, S. 2012 Selected physiological effects of ultrafine particles in acute cardiovascular morbidity. *Environ. Res.* **115**, 26–36.
- Williams, D. M. & Rubin, B. K. 2018 Clinical pharmacology of bronchodilator medications. *Respir. Care* **63** (6), 641–654.